Geological evidence confirms the staircase patterns of Earth's rotation deceleration from the Neoproterozoic to the Mesozoic Era

He Huang[1,2,3], Chao Ma[1,2,*], Matthias Sinnesael[3], Mohammad Farhat[3], Nam H. Hoang[3], Yuan Gao[4], Christian Zeeden[5], Hanting Zhong[1,2], Mingcai Hou[1,2], Chengshan Wang[4], Jacques Laskar[3]

[1] State Key Laboratory of Oil and Gas Reservoir Geology and Exploitation, Institute of Sedimentary Geology, Chengdu University of Technology, Chengdu 610059, China

[2] Key Laboratory of Deep-time Geography and Environment Reconstruction and Applications of Ministry of Natural Resources, Chengdu University of Technology, Chengdu 610059, China

[3] IMCCE, CNRS, Observatoire de Paris, PSL University, Sorbonne Université, 75014, Paris, France

[4] State Key Laboratory of Biogeology and Environmental Geology, China University of Geosciences (Beijing), Beijing 100083, China

[5] LIAG-Leibniz Institute for Applied Geophysics, Stilleweg 2, 30655 Hannover, Germany

Corresponding author: Chao Ma

Email: machao@cdut.edu.cn

Abstract

Due to tidal dissipation, the Earth's rotation has been slowing down, but the past rates of this process remain subject of debate. Here we conducted a comprehensive cyclostratigraphic analysis of eight geological datasets to further constrain the Earth's rotation history from the Neoproterozoic to Mesozoic. Our results allow us to further test theoretical physical tidal models, and support a suggested stair-shaped Earth's rotation deceleration pattern during 650-280 Ma, thereby increasing the Earth-Moon distance about 20,000 km and the length of solar day approximately 2.2 hours. Specifically, the high rate of Earth's rotation deceleration from 650 Ma to 500 Ma can be attributed to the enhanced tidal resonance. In contrast, the unusually low tidal dissipation during 500-350 Ma has led to a flatter trend of Earth's rotation deceleration, closely followed by another high rate of Earth's rotation deceleration during 350-280 Ma. These changes in Earth's rotation are closely linked to alterations in Earth's tectonic contexts and ocean tidal resonance. Hence, we speculate that there might be a relationship between the Earth's rotation and geological processes.

Keywords: Earth-Moon system, Earth's rotation, cyclostratigraphy, tidal resonances, geological processes

Introduction

Due to the tidal interplay in the Earth-Moon system, and by virtue of angular momentum conservation, the Earth's rotational angular momentum is transferred to the orbital counterpart of the Moon (1). Consequently, the deceleration of Earth's rotation and the gradual orbital recession of the Moon constitute an ongoing process that has persisted since the formation of the Earth-Moon system to the present day. However, the deceleration rate of Earth's rotation has changed over time and appears to have exhibited a nonlinear pattern, as suggested by geological observations (2-5). The Earth's rotational motion can be described by its axial precession frequency, which gives the change in orientation of the spin in arc seconds per year (arcsec/yr, denoted as *p* following ref. (6)). The present value of *p* is measured with high precision (50.475838 arcsec/yr) (6), but the evolution history of the Earth's rotational motion is largely unknown. Apollo's Lunar laser ranging (LLR) observations of today's Lunar recession rate (~3.83 cm/yr) (7) and the age of the Moon (~4.425 billion years ago (Ga)) (8) provide two constraints on Lunar recession history. However, combining the models of bodily tides with the present LLR measurements, one would predict a collision between the Moon and Earth at ~1.5 Ga (9, 10), which is obviously incompatible with the lunar age inferred from radioisotopic dating analyses (8, 11, 12). Several studies have proposed various solutions to solve this paradox by using analytical models, numerical simulations and observational geological data (10, 13-16). However, as the current theoretical tidal models are short of being comprehensive in describing dissipative processes, reliable observational geological data are crucial for further constraining theoretical model predictions.

Over the past few decades, a series of empirical geological records have been reported to reconstruct the Earth’s astronomical properties, such as the number of days per lunar month inferred from tidalites (5, 17, 18), and the number of days per solar year calculated from growth rings of invertebrate fossils (2, 19-22). Although the analysis of tidalites and invertebrate fossils is undoubtedly meaningful and improves our understanding of the Earth's rotation history (23), both of them exhibit large uncertainties in cycle interpretation and counting (5, 23-25), which might result in inconsistencies with the true situation of Earth’s rotational properties and even give incorrect reconstruction of the Earth-Moon evolution (review in ref. 24). For instance, the Lunar semimajor axis deduced from Weeli-wolli tidal rhythmites at 2450 Ma ago were interpreted differently by Walker and Zahnle (26), and Williams (5). Walker and Zahnle identified them as indicative of Lunar nodal precession, whereas Williams interpreted the periodic sedimentary features as representative of spring-neap tides occurring within an annual cycle. Similar incompatible interpretations of the same record can also be noticed in the case of the Cottonwood tidal rhythmites at 900 Ma (17, 27) and the Elatina tidal rhythmites at 620 Ma (5, 17, 28).

With recent developments in cyclostratigraphy, we can extract the Earth’s astronomical properties from astronomically-forced stratigraphic records using more robust quantitative methods (29-31). Consequently, over the past years, numerous *p* values accompanied by uncertainty estimations have been reported (29-35). These contributions have substantially enriched our understanding of the history of Earth-Moon evolution. To date, it seems that astronomically-forced cyclostratigraphic records might be the most robust archives for deciphering past changes in Earth's rotation and Lunar recession history (24), especially if amplitude relationships between precession and eccentricity can be demonstrated. However, it remains essential to continue gathering reliable geological data to independently test physical tidal models. This is particularly crucial in the critical periods that align with modeled prediction of significant astronomical variations that are driven by oceanic tidal resonances (16) or the atmospheric thermal tidal locking hypothesis during the boring billion period (1.8-0.8 Ga) (24, 36). Here, we use the Monte Carlo Markov Chain (MCMC) Bayesian inversion method developed by ref. (29) (i.e., TimeOptMCMC, see Methods) to compute the *p*-values from eight high-fidelity cyclostratigraphic time series covering ages ranging from 245 Ma to 570 Ma (32, 37-43) (*SI Appendix*, Table S1, Fig. S1-S8). These new *p*-values, along with other published *p*-values, have nicely constrained the Earth's rotation history from the Neoproterozoic to the Mesozoic Era and served as an independent way to test the theoretical physical tidal models.

Results

Cyclostratigraphic datasets compilation

Through multiple cyclostratigraphic analyses and tests (see Methods), we identified eight high-fidelity datasets from the literature (excluding those analyzed by refs. (29, 34)) that were suitable for TimeOptMCMC analysis (the detailed analysis parameters refer to *SI Appendix*, Table S1 and Supplementary R scripts). The detailed information of these datasets is as follows: **(Ⅰ)** The Guandao section was deposited in a marine environment during the latest Permian through the earliest Late Triassic (36). A ~260 m gamma ray (GR) data was retrieved from this section for cyclostratigraphic analysis (37). Variations in GR relate to the terrestrial input and marine productivity, which controlled by the astronomical forcing (37). We chose the

10-72 m interval (~245 Ma) to run the TimeOptMCMC simulation. **(Ⅱ)** The Permian Lucaogou Formation (~290 Ma) developed in a lacustrine environment, and mainly consisting of shale facies with thin beds of dolomitic siltstone as a minor lithology. The log natural gamma ray (GR) data show strong variations associated with the orbital forcing (32). We chose the 3650-3770 m interval to perform the TimeOptMCMC analyses. **(Ⅲ)** The H-32 drilling core in Iowa recorded a positive $\delta^{13}C$ excursion associated with the Frasnian–Famennian (F–F) boundary during the Upper Devonian (38*)*. The magnetic susceptibility (MS) data revealed quasi-periodic signals at eccentricity, obliquity and precession bands (38). Although the precession band signals are not obvious (Fig. S3), we still chose the 1.76-9 m interval (~375 Ma) for TimeOptMCMC analyses. This choice was necessitated by the absence of any other available cyclostratigraphic dataset capable of reconstructing Earth's rotation rate within the time frame spanning from 290 Ma to 410 Ma (Figs. 1, 2). Consequently, it plays a crucial role in constraining potential trends in Earth's rotation deceleration trajectory during this period, although the reconstructed *p*-value features a relatively high uncertainty (Table 1). **(Ⅳ)** The Požár-CS limestone section has a thickness of 118 m, covering the Lochkov and Praha Formations. High resolution MS was measured from this section by Da Silva et al. (39). Cyclostratigraphic analyses of the MS data revealed obvious Milankovitch signals (39). We chose the 106.7-114 m interval (~410 Ma) for TimeOptMCMC analyses. **(Ⅴ)** In Anticosti Island, Canada, a remarkably well-preserved and substantial Upper Ordovician reference section was deposited within a structural embayment situated along the eastern margin of Laurentia. The Vauréal Formation, belonging to the upper Katian Stage primarily comprises interbedded micrite, calcarenite, and marl, exhibiting astronomically-forced lithological associations (40). High-resolution potassium (K%) was measured for reflecting the multimeter cycles of carbonate versus clay lithology (40). Here, we chose the 550-900 m interval (~448 Ma) for the TimeOptMCMC analysis. **(Ⅵ)** The Liangjiashan section, located along the margin of the North China Block, represents the deposition of shallow marine carbonate during the Early Ordovician period. A set of 1024 geochemical data points derived from X-ray fluorescence (XRF) analysis was obtained at the Liangjiashan section (41). These data encompassed the elemental composition of Ti, Si, Fe, and Ca. Milankovitch cycles have been identified in the Liangjiashan section by analyzing the Ca% (41). Here, we chose the 45-62 m interval (~470 Ma) for the TimeOptMCMC analyses. **(Ⅶ)** The Alum Shale Formation is primarily composed of laminated, organic-rich mudstone characterized by a substantial presence of pyrite. The elemental abundances retrieved from high resolution core scanning XRF analysis (42). By analyzing the S% composition, a floating timescale calibrated to the stable 405 kyr eccentricity cycle was established for an approximately 8.7 Ma interval spanning the Miaolingian-Furongian boundary (42). Here, we chose the 83-85.5 m (~493Ma) interval for TimeOptMCMC analyses. **(Ⅷ)** The Doushantuo Formation was deposited on the inner shelf of the Ediacaran Yangtze Platform at the Zhengjiatang section. Within this section, high-resolution MS series were obtained from the stratigraphic interval containing the Shuram carbon isotope excursion (CIE) (43). Power spectral analyses conducted on the MS series of the carbonate rocks demonstrate periodicities that align closely with the Milankovitch cycles at ~570 Ma (43). Here, we chose the 26-33 m interval to perform the TimeOptMCMC analyses.

The TimeOptMCMC analysis results

By running the TimeOptMCMC analysis, the prior distributions of the sedimentation rate (SR) inherited from the original literature and also further independently constrained by the TimeOpt analysis, while the *p* ranges were obtained from the tidal model of Waltham (13) (see Methods, *SI Appendix*, Table S2). The TimeOptMCMC results of eight cyclostratigraphic time series are shown here (Table 1, Fig. 1). The blue histograms depict the posterior distributions of the SR and *p*, while prior distributions are in grey (Fig. 1). Comparing the two distributions, it becomes evident that the posterior distributions are more confined compared to the prior distributions (Fig. 1). This outcome signifies the successful optimization of SR, *p*, and the fundamental secular frequencies g_i terms by the TimeOptMCMC. The mean value and standard deviation (σ) of SR and *p* were calculated from the after burn-in results from the MCMC simulation results (Table 1). According to the *p* value, we can derive the Earth-Moon distance (EMD), the length of the solar day (LOD) and Earth's obliquity angle according to the model of Farhat et al. *(16)* using the tool provided on the *AstroGeo* website (http://www.astrogeo.eu/) (Table 1, *SI Appendix*, Fig. S10). For example, the TimeOptMCMC analysis generates a posterior distribution that determines Earth precession rate at 56.70 ± 2.26 arcsec/yr at 245 Ma (Table 1). This observation is consistent with an EMD of 373.99 (+3.36/-3.22) thousand kilometers, a day length of 22.63 (+0.46/-0.45) hours and an average obliquity angle at 22.62 (+0.21/-0.21) degree (Table 1). Similarly, Table 1 presents the TimeOptMCMC results for all here analyzed datasets.

The change-point analysis results

In addition, we have integrated our new dataset into the published cyclostratigraphically derived *p*-values spanning from approximately 200 Ma to 700 Ma (Fig. 2). We have also employed change-point analysis (44) (see Methods) to identify the trends of evolution among these reconstructed *p*-values (Fig. 2). This method has divided these data into three distinct groups which reveal two notable shifts in Earth's rotation deceleration intervals (Fig. 2, *SI Appendix*, Fig. S9). The first substantial shift in Earth's rotation deceleration occurred between ~280 Ma and ~350 Ma, representing the first high slope (Fig. 2). The second high slope, indicating another abrupt change in Earth's rotation deceleration, began around ~480 Ma (Fig. 2). Specifically, the first group comprises three data points, resulting in a linear deceleration rate of approximately 0.0068 arcsec/Ma. Conversely, the second group, encompassing five data points, does not display a discernible downward trend within this dataset. Finally, the last group, which also consists of five data points, exhibits a pronounced linear downward trend. In this case, we calculate a linear deceleration rate of 0.059 arcsec/Ma, surpassing the rate observed in the first group. Overall, our newly acquired data along with published data suggest a nonlinear staircase variation pattern in Earth's rotation deceleration from 700 Ma to 200 Ma (Fig. 2, *SI Appendix*, Fig. S9).

Discussion

Comparison of our new geological constraints with tidal models

Previous studies have proposed a series of models to reconstruct the evolution of the Earth-Moon system based on the tidal theory of solid and fluid bodies (6, 10, 13-16, 45, 46). While these models provide valuable insights, they vary significantly in the underlying assumptions, constraints, and the approach of obtaining the tidal solution. Consequently, they offer a wide range of possible evolutionary tracks of the Earth-Moon system (Fig. 3b). Therefore, geological observations provide an independent way to constrain the Earth-Moon evolution and test the reliability of these models. In what follows, we compare our new geological findings with five models, namely the La04 (6), W15 (13), T21 (15), D21 (14) and F22 (16) models (Fig. 3).

The La04 tidal model is based on the constant time lag assumption (47), where the time it takes the Earth to establish its equilibrium state after the lunar tidal stress is fixed. This assumption is valid when describing the system at present and closely in the past, but fixing the time lag over geological timescales is unjustified given the evolving response of the paleo-oceans. As such, and since the present state of the ocean system corresponds to anomalously high tidal dissipation, the La04 model overestimates the lunar recession rate in the past. Therefore, the Earth's precession frequency in the La04 model shows a higher value in comparison with the rest of the models, as well as the geological records (Fig. 3b). Waltham (13) reconstructed the history of the Earth-Moon separation by employing two fixed endpoints, specifically 384 thousand km at the present and approximately 30 thousand km (Roche limit distance) at 4.5 Ga. Clearly, the W15 model reports a higher degree of uncertainty in determining the Earth's precession frequency due to the limited availability of effective constraint parameters. Consequently, nearly all of the geological records align with the Earth's precession frequency ranges depicted in the W15 model, but we note that these data are more concentrated toward the higher end of the range, and those that do not fall within the range are always above it (Fig. 3b).

Recent advances in tidal theory, especially for fluid tides, has facilitated the formulation of more refined and physically grounded models. The present state-of-the art models are: T21 (15), D21 (14), and F22 (16) (Fig. 3c). The T21 model adopts a global ocean configuration which persists over the lifetime of the Earth-Moon system, and is parameterized by two free parameters: an effective oceanic thickness and a timescale of tidal dissipation (15). These two parameters were constrained by fitting the reconstructed system history to the geological data available at the time (which mainly correspond to tidal rhythmites and paleontological clocks). Through comparison with the geological data, we have found that the T21 model exhibits a good fit during the past 300 Ma, while beyond 300 Ma, the model results show an increasing discrepancy with geological data (Fig. 3c). In contrast, Daher et al. (14) used a numerical approach to compute the tidal solution by using four different ocean geometry conditions, specifically the present-day (PD) ocean basin geometry and with 55 Ma, 116 Ma, and 252 Ma reconstructed basin paleogeometries. The PD continental configuration and mean sea level value result in unusually larger tides both in open-ocean and coastal regions than most periods of geological history (14, 48). Evidently, the D21-PD tidal dissipation rate overestimated the past tidal dissipation, while during 600-1000 Ma, the tidal dissipation rate is similar to the PD condition (Fig. 3c). The tidal simulation results for D21-55 and D21-116 exhibit a similar trend to D21-PD but demonstrated a better fit with the geological data for the past 100 Ma (Fig. 3c). The D21-252 tidal simulation underestimates the past tidal dissipation rate, resulting in a longer LOD than geological observations (Fig. 3c). Furthermore, Green et al. (48) also modelled the tidal energy around 252 Ma, and found that the total dissipation rates was much lower than present levels.

Recently, Farhat et al. (16) presented a semi-analytical physical tidal model that utilizes two parameters to characterize the ocean: the average ocean depth (H) and a dissipation factor (σ_R). These parameters were tuned such that the reconstructed tidal history fits well with the current tidal recession rates and the Moon’s age. While geological data were not incorporated into the model's development, the latter independently aligns well with historical Earth-Moon distance estimations, particularly in concordance with geological constraints derived from cyclostratigraphic techniques (16). Here, we also see a higher degree of similarity between our new *p* data and previously published geological data, and the F22 tidal model compared to the other theoretical models (Fig. 3). In the F22 model, the Earth-Moon tidal evolution is simulated through three distinct phases, with each phase corresponding to a different ocean model (namely, global and hemispherical oceans) as well as distinct plate tectonic backgrounds since 1 Ga (16). As such, the F22 model took into account the effect of continentality, which was absent in the T21 model, and the effect of evolving surface geometry in a single reconstructed history, which is different from the D21 model. This is probably the potential reason for the better agreement between our geological findings and F22 model.

Staircase patterns of Earth's rotation deceleration

By integrating our new datasets with previously published geological findings, we have observed a notable Earth's rotation deceleration period at 650-500 Ma, which is comparable with the F22 model (Figs. 2, 3b, *SI Appendix*, Fig. S9). During this time interval, the *p* value experienced a clear reduction from approximately 70 arcsec/yr to around 60 arcsec/yr (Figs. 2, 3b). This deceleration period roughly corresponds to the termination of the Cryogenian glaciations, which may imply that more of Earth's surface was affected by ocean inundation and consequently an intensification in tidal friction (49-51) (*SI Appendix*, Fig. S11b, c, d). During this period, there has been a notable increase in the length of continental arcs, the extent of shallow marine areas and the depth of seawater on continental shelves (*SI Appendix*, Fig. S11b, c, d). The augmented shallow marine regions play a crucial role in governing the tidal dissipation rate since tidal energy dissipation primarily occurs within these areas (14, 48).

Additionally, during the time period of 500-350 Ma, the new *p*-values derived from geological data show a relatively stable trend (Fig. 3b). This trend, however, is consistently below the predicted evolution in the F22 model (Fig. 3b). The latter signature could be due to our chosen prior on *p* ranges from Waltham model (13). Namely, while the staircase patten is a robust feature of our geological inferences, the absolute position of this pattern on the precession frequency scale is dependent on the chosen prior. Therefore, the fact that the F22-modeled curve lives around the upper limit of our prior distribution can explain the slight offset between the curve and our findings. The gentle trend is located between two high slopes and further validates the staircase shape of the p variations from ~650 Ma to ~280 Ma (Figs. 2, 3b). During this period, we also notice that two p data points (Fig. 3b) derived from Zeeden et al. (31) and Zhong et al. (52) exhibit clear inconsistency with our new geological observations and the F22 tidal model (31, 52). The cyclostratigraphic analysis conducted by Zhong et al. (52) only relies on the main obliquity component ($p+s_3$, s_3 represents the precession of node of the Earth) for calculating the p value. By comparing their result with the tidal models and the majority of geological estimates, their result appears to be inconsistent (31) (Fig. 3b). In order to test the data point of Zeeden et al (31), we compared the variation trends from different datasets (*SI Appendix*, Fig. S9). We have found that although the point of Zeeden et al (31) does not have a clear influence on the trend of 650-500 Ma interval, it has a significant impact on another deceleration period from 350-280 Ma (*SI Appendix*, Fig. S9). Consequently, the data point of Zeeden et al (31) plays a crucial role in constraining the staircase patterns of the Earth’s rotation deceleration history from 200 Ma to 700 Ma.

In the F22 model (16), there is another deceleration period from 350 Ma to 280 Ma (Fig. 3). For this time interval, the large uncertainty associated with the new geological estimate at 375 Ma in terms of the p-value, coupled with the lack of sufficient geologically-derived p values from this interval, poses a substantial challenge in determining the true trend of the changes on Earth’s rotation rate (Fig. 3b, *SI Appendix*, Fig. S9). However, if we take account into the data point from Zeeden et al (31), we can nicely recover the evolution of this deceleration period (Fig. 2 and *SI Appendix*, Fig. S9). As such, though our dataset provides discrete snapshots of the evolution history at an unprecedented resolution, which are further in good agreement with the F22 model, we maintain the belief that a conclusive and comprehensive description of this interval still requires additional high-quality geological datasets along with improved quantitative analysis methods.

The geological relevance of the Earth's rotation deceleration

The tidal dissipation (1) and Earth dynamic ellipticity (53, 54) are the main driver of changes in the Earth's rotation. Both of them are causally linked to the tectonic and climatic evolution of the Earth. Hence, a correlation between Earth's rotation and some specific geological processes may be anticipated (*SI Appendix*, Figs. S11-S13). Although their interactions are complex and not fully understood, several potential connections have been proposed (2, 47, 55, 56). In this study, the Earth rotation deceleration was accompanied by a rapid increase in the average of Earth's obliquity angle (from ~21.6° to ~22.6°, present day mean obliquity is 23.25°) from ~650 Ma to 280 Ma (Table 1, *SI Appendix*, Fig. S10). This substantial shift in obliquity may serve as a triggering factor for the development of Earth's glacial periods (e.g., Late Paleozoic Ice Age). In addition, changes in day length (*SI Appendix*, Fig. S10), for instance, can influence the distribution of Solar energy and temperature gradients, potentially impacting weather systems and atmospheric dynamics (57). Interestingly, we also observe that the first oceanic tidal resonance coincides with the Neoproterozoic oxygenation event (NOE, ~600 Ma) (58) and the Cambrian explosion (59) (*SI Appendix*, Fig. S12), while the second resonance aligns with both the Phanerozoic oxygenation event (POE, ~350 Ma) and late Carboniferous to early Permian biodiversification event (*SI Appendix*, Fig. S12). Therefore, it is important to consider a potential connection between the changes of LOD and the evolution of ocean circulation and ecosystems (56, 60).

Methods

Evaluation and screening of the published cyclostratigraphic datasets

In this study, we have compiled a wide range of cyclostratigraphic time series from published papers (references herein). Firstly, these cyclostratigraphy data are used to estimate the SR based on the independent age model provided in their original text (*SI*

Appendix, Table S2), thereby establishing a prior hypothesis for the sedimentation rate range used in the following astronomical cycle interpretations, TimeOpt and TimeOptMCMC analysis. Secondly, the Evolutionary Fast Fourier Transform (eFFT) analysis is applied to identify the most significant and stable interval of astronomical cycle signals, with particular emphasis on precession and eccentricity signals. Subsequently, for a promising subselection of case based on the eFFT analyses, the TimeOpt method is employed to investigate the amplitude modulation relationship between precession and eccentricity signals and to determine the optimal sedimentation rate and duration within the chosen interval (*SI Appendix*, Figs. S1-S8). Finally, the decision to perform the TimeOptMCMC analysis is based on the r^2_{opt} and P values obtained from TimeOpt (*SI Appendix*, Table S1).

TimeOpt and TimeOptMCMC analysis

Following the approach of ref. (29), all of these selected geological data were firstly tested using the TimeOpt method with prior climatic precession and eccentricity periods to test for an astronomical signal under a relatively wide range of sedimentation rate models. The prior of SR ranges were derived from the original articles (reference herein, *SI Appendix*, Table S2). The statistically significant TimeOpt results (r^2_{opt}, p value; *SI Appendix*, Figs.S1-S8, Table S1) are an important prerequisite for running the MCMC optimization. Bayesian inversion of these geological records are constrained by prior distributions for the fundamental frequencies g_1 to g_5, the precession frequency p, and SR (*SI Appendix*, Table S2). Prior distributions for the fundamental frequencies g_1 to g_5 are based on the full range of variability in the model simulations of Laskar et al. computed over 500 My (6). The prior distribution for the precession frequency is derived from the study by Waltham (13), which provides a relatively wide range of possibility. Importantly, in this study, we need to note that the different choice of the prior distribution could slightly affect the outcomes of the TimeOptMCMC analysis, but the variation pattern of our datasets is robust, which is independent from the prior distribution. For different cyclostratigraphic datasets, we have run different number of MCMC chains and samples (*SI Appendix*, Table. S1), and then we extracted the post burn-in results of all MCMC chains to calculate the mean value of each parameter with its standard deviation (±σ). For more detailed information about the TimeOpt and TimeOptMCMC methods refer to refs. (29).

Change-point analysis

A changepoint is a sample or time instant at which some statistical property (for instance: mean value, standard deviation, trend) of a signal changes abruptly (44). The MATLAB function ‘findchangepts’ can be used to detect the change points in a time series. We have employed this function to estimate the “linear” statistic properties of the cyclostratigraphically derived *p*-values time span from 200 Ma to 700 Ma (Fig. 2). To display the abrupt changes on these data, we plot the linear regression lines of different data groups and calculate the mean slope of all regression lines (Fig. 2). In summary, our statistical analysis suggests the presence of two discernible change points/intervals (~280-350 Ma, ~480 Ma) based on these data (Fig. 2; *SI Appendix*, Fig.S9).

Acknowledgments

We thank Zhisong Cao, Hang He and Tianyu Huang for help with performing the TimeOptMCMC and Change-point analyses. We thank Yuyin Li for help with preparing figures and tables. We are grateful for Stephen R. Meyers’ valuable suggestions on our preliminary draft. We thank editors and reviewers for helpful and constructive comments. This work was financially supported by the National Natural Science Foundation of China (grants no. 41888101, 42172137, 42302122, 42050104 and 42050102), Sichuan Provincial Youth Science & Technology Innovative Research Group Fund (No. 2022JDTD0004) and European Research Council (ERC) under the European Union’s Horizon 2020 Research and Innovation Program (Advanced Grant AstroGeo-885250). H.H thanks Chengdu University of Technology (CDUT) provides the financial support (Grant No. 21700-000504) for visiting the IMCCE, CNRS, Observatoire de Paris, France. This study is a contribution to the

Deep-time Digital Earth (DDE) Big Science Program. Moreover, this study benefited from the researchers who made their research code (Astrochron software; Meyers, 2014) and original data accessible.

References

1. G.A. Darwin, A tidal theory of the evolution of satellites. Observatory 3, 79–84 (1879).

2. C. M. G. Pannella, M. N. Thompson, 1968. Paleontological Evidence of Variations in Length of Synodic Month since Late Cambrian. Science. 162, 792-796 (1968).

3. B.G. Bills, R.D. Ray, Lunar orbital evolution: A synthesis of recent results. Geophysical Research Letters. 26, 3045-3048 (1999).

4. E.P. Kvale, H.W. Johnson, C.P. Sonett, A.W. Archer, A. Zawistoski, Calculating lunar retreat rates using tidal rhythmites. Journal of Sedimentary Research. 69, 1154-1168 (1999).

5. G. E. Williams, Geological Constraints on the Precambrian History of Earth's Rotation and the Moon's Orbit. Rev. Geophys. 38, 37–59 (2000).

6. J. Laskar, P. Robute, F. Joutel, M. Gastineau, A. C. M. Correia, and B. Levrard, A long-term numerical solution for the insolation quantities of the Earth. Astron. Astrophys. 428, 261–285 (2004).

7. J.G.Williams, D.H. Boggs, Secular tidal changes in lunar orbit and Earth rotation. Celest. Mech. Dyn. Astron, 126, 89–129 (2016).

8. M. Maurice, N. Tosi, S. Schwinger, D. Breuer, T. Kleine, A long-lived magma ocean on a young Moon. Sci. Adv., 6, eaba8949 (2020).

9. H. Gerstenkorn, On the controversy over the effect of tidal friction upon the history of the earth-moon system. Icarus, 7, 160–167 (1967).

10. J. Webb, Tides and the evolution of the Earth-Moon system. Geophys. J. R. Astron. Soc. 70, 261–271 (1982).

11. F. Tera and G.J. Wasserburg, U-Th-Pb systematics in lunar highland samples from the Luna 20 and Apollo 16 missions. Earth and Planetary Science Letters, 17, 36-51 (1972).

12. M. Barboni, P. Boehnke, B. Keller et al., Early formation of the Moon 4.51 billion years ago. Sci. Adv., 3, e1602365 (2017).

13. D. Waltham, Milankovitch period uncertainties and their impact on cyclostratigraphy. J. Sediment. Res. 85, 990–998 (2015).

14. H. Daher et al., Long-term Earth-Moon evolution with high-level orbit and ocean tide models. J. Geophys. Res. Planets. 126, e2021JE006875 (2021).

15. R. H. Tyler, On the tidal history and future of the Earth–Moon orbital system. Plan. Sci. J. 2, 70 (2021).

16. M. Farhat, P. Auclair-Desrotour, G. Boue, J. Laskar, The resonant tidal evolution of the Earth-Moon distance. Astron. Astrophys. 665, L1 (2022).

17. C. P. Sonett, M. A. Chan, Neoproterozoic Earth-Moon dynamics: Rework of the 900 Ma Big Cottonwood Canyon tidal laminae. Geophysical Research Letters, 25, 539–542, (1998).

18. T. Eulenfeld and C. Heubeck, Constraints on Moon's Orbit 3.2 billion years ago from tidal bundle data. Journal of Geophysical Research: Planets. 128, e2022JE007466 (2023).

19. J. W. Wells, Coral growth and geochronometry. Nature. 197, 948-950 (1963).

20. K. Lambeck, The Earth's Variable Rotation (Cambridge University Press, 1980).

21. J. P. Vanyo, S. M. Awramik, Stromatolites and Earth–Sun–Moon dynamics. Precambrian Research, 29, 121–142 (1985).

22. N.J. de Winter, S. Goderis, V. Malderen, M. Sinnesael, S. Vansteenberge, C. Snoeck, J. Belza, F. Vanhaecke, P. Claeys, Subdaily-Scale Chemical Variability in a *Torreites Sanchezi* Rudist Shell: Implications for Rudist Paleobiology and the Cretaceous Day-Night Cycle. Paleoceanography and Paleoclimatology. 35 (2020).

23. S. D. Deines, C. A. Williams, Earth's Rotational Deceleration: Determination of Tidal Friction Independent of Timescales. The Astronomical Journal. 151, 103 (2016).

24. J. Laskar, M. Farhat, M. Lantink, P.auclair-Desrotour, G. Bou´e, M. Sinnesael, Did atmospheric thermal tides cause a daylength locking in the Precambrian? A review on recent results. arXiv:2309.11479 (2023). https://doi.org/10.48550/arXiv.2309.11479

25. C. Heubeck, S. Biasing, M. Grund, N. Drabon, M. Homann, S. Nabhan, Geological constraints on Archean (3.22 Ga) coastal-zone processes from the Dycedale Syncline, Barberton Greenstone Belt. South Afr. J. Geol., 119, 495–518 (2016).

26. J. C. Walker, K. J. Zahnle, Lunar nodal tide and distance to the Moon during the Precambrian. Nature, 320, 600-602 (1986).

27. C. P. Sonett, E. P. Kvale, A. Zakharian, M. A. Chan, T. M. Demko, Late Proterozoic and Paleozoic tides, retreat of the Moon, and rotation of the Earth. Science, 273(5271), 100-104 (1996).

28. G. E. Williams, Precambrian length of day and the validity of tidal rhythmite paleotidal values. Geophysical Research Letters, 24(4), 421-424(1997).

29. S. R. Meyers, A. Malinverno, Proterozoic Milankovitch cycles and the history of the solar system. Proc. Natl. Acad. Sci. U.S.A. 115, 6363–6368 (2018).

30. M. L. Lantink, J. Davies, M. Ovtcharova, F. J. Hilgen, Milankovitch cycles in banded iron formations constrain the Earth-Moon system 2.46 billion years ago. Proc Natl Acad Sci U.S.A. 119, e2117146119 (2022).

31. C. Zeeden, J. Laskar, D. V Vleeschouwer, D. Pas, A.C. Da Silva, Earth's rotation and Earth-Moon distance in the Devonian derived from multiple geological records. Earth Planet. Sci. Lett. 621, 118348 (2023).

32. H. Huang, Y. Gao, M. M. Jones, H. Tao, A. R. Carroll, D. E. Ibarra, H. Wu, C. Wang, Astronomical forcing of Middle Permian terrestrial climate recorded in a large paleolake in northwestern China. Palaeogeography, Palaeoclimatology, Palaeoecology. 550, 109735 (2020).

33. T. Zhang, Y. Li, T. Fan, A. C. Da Silva, J. Shi, Q. Gao, M. Kuang, W. Liu, Z. Gao, M. Li, Orbitally-paced climate change in the early Cambrian and its implications

for the history of the Solar System. Earth Planet. Sci. Lett. 583, 117420 (2022).

34. M. Zhou, H. Wu, L. A. Hinnov, Q. Fang, S. Zhang, T. Yang, M. Shi, Empirical Reconstruction of Earth-Moon and Solar System Dynamical Parameters for the Past 2.5 Billion Years From Cyclostratigraphy. Geophysical Research Letters. 49 (2022).

35. D. De Vleeschouwer, D. E. Penman, S. D'Haenens, F. Wu, T. Westerhold, M. Vahlenkamp, C. Cappelli, C. Agnini, W.E.C. Kordesch, D.J. King, R. van der Ploeg, H. Pälike, S. K. Turner, P. Wilson, R. D. Norris, J. C. Zachos, S. M. Bohaty, P. M. Hull, North Atlantic Drift Sediments Constrain Eocene Tidal Dissipation and the Evolution of the Earth-Moon System. Paleoceanography and Paleoclimatology. 38 (2023).

36. K. J. Zahnle, J. C. G. Walker, A constant daylength during the Precambrian era? Precambrian Res, 37: 95-105 (1987).

37. M. Li, C. Huang, L. Honnov, W. Chen, J. Ogg, W. Tian, Astrochronology of the Anisian stage (Middle Triassic) at the Guandao reference section, South China. Earth Planet. Sci. Lett.,482, 591-606 (2018).

38. D. De Vleeschouwer, A.C. Da Silva, M. Sinnesael, D. Chen, J.E. Day, M.T. Whalen, Z. Guo, P. Claeys, Timing and pacing of the Late Devonian mass extinction event regulated by eccentricity and obliquity. Nature Communications. 8 (2017).

39. A.C. Da Silva, J. Hladil, L. Chadimová, L. Slavík, F.J. Hilgen, O. Bábek, M.J. Dekkers, Refining the Early Devonian time scale using Milankovitch cyclicity in Lochkovian–Pragian sediments (Prague Synform, Czech Republic). Earth and Planetary Science Letters. 455, 125-139 (2016).

40. M. Sinnesael, P.I. McLaughlin, A. Desrochers, A. Mauviel, J. De Weirdt, P. Claeys, T.R.A. Vandenbroucke, Precession-driven climate cycles and time scale prior to the Hirnantian glacial maximum. Geology (2021).

41. K. Ma, R. Li, L.A. Hinnov, Y. Gong, Conodont biostratigraphy and astronomical tuning of the Lower-Middle Ordovician Liangjiashan (North China) and Huanghuachang (South China) marine sections. Palaeogeography Palaeoclimatology Palaeoecology. 528, 272-287 (2019).

42. A. L. Sørensen, A. T. Nielsen, N. Thibault, Z. Zhao, N.Schovsbo, T. W. Dahl,

Astronomically forced climate change in the late Cambrian. Earth Planet. Sci. Lett. 548, 116475 (2020).

43. H. Li, S. Zhang, J. Han, T. Zhong, J. Ding, H. Wu, P. Liu, J. Dong, Z. Zhang, T. Yang, G. Jiang, Astrochronologic calibration of the Shuram carbon isotope excursion with new data from South China. Global and Planetary Change. 209, 103749 (2022).

44. Killick, R., Eckley, I. A., changepoint: An R Package for Changepoint Analysis. Journal of Statistical Software. 58 (3), 1-19 (2014).

45. K. S. Hansen, Secular effects of oceanic tidal dissipation on the Moon's orbit and the Earth's rotation. Rev. Geophys. Space Phys. 20, 457–480 (1982).

46. A. Berger, M. F. Loutre, J. Laskar, Stability of the astronomical frequencies over the Earth's history for paleoclimate studies. Science 255, 560–566 (1992).

47. F. Mignard, The evolution of the lunar orbit revisited. I. The Moon and the planets, 20(3), 301-315 (1979).

48. J. A. M. Green, M. Huber, D. Waltham, J. Buzan, M. Wells, Explicitly modelled deep-time tidal dissipation and its implication for Lunar history. Earth Planet. Sci. Lett. 461, 46–53 (2017).

49. W. Cao, C. T. A. Lee, J.S. Lackey, Episodic nature of continental arc activity since 750 Ma: a global compilation. Earth Planet. Sci. Lett. 461, 85–95 (2017).

50. S.E. Peter and J.M. Husson, Sediment cycling on continental and oceanic crust. Geology (2016).

51. R.D. Nance, J.B. Murphy, M. Santosh, The supercontinent cycle: A retrospective essay. Gondwana Research. 25, 4-29 (2014).

52. Y. Zhong, H. Wu, J. Fan, Q. Fang, M. Shi, S. Zhang, T. Yang, H. Li, L. Cao, Late Ordovician obliquity-forced glacio-eustasy recorded in the Yangtze Block, South China. Palaeogeogr. Palaeoclimatol. Palaeoecol., 540, 109520 (2020).

53. L. J. Lourens, R. Wehausen, H. J. Brumsack, Geological constraints on tidal dissipation and dynamical ellipticity of the Earth over the past three million years.

Nature, 409(6823), 1029-1033 (2001).

54. M. Farhat, J. Laskar, G. Boué, Constraining the Earth's Dynamical Ellipticity From Ice Age Dynamics. Journal of Geophysical Research: Solid Earth, 127, 1-22 (2022).

55. W.R. Peltier, Postglacial variations in the level of the sea: Implications for climate dynamics and solid-Earth geophysics. Reviews of Geophysics. 36, 603-689 (1998).

56. J. M. Klatt, A. Chennu, B. K. Arbic, B. A. Biddanda, G. J. Dick, Possible link between Earth's rotation rate and oxygenation. Nat. Geosci. 14, 564–570 (2021).

57. S.J. Gregory, G.M. Hal, W.R. Kuhn, Precambrian Climate: The Effects of Land Area and Earth's Rotation Rate. J. Geophys. Res. 98, 8785-8791 (1993).

58. T.W. Lyons, C.T. Reinhard, N.J. Planavsky, The rise of oxygen in Earth's early ocean and atmosphere. Nature. 506, 307-315 (2014).

59. J. Fan, S. Shen, D.H. Erwin, P.M. Sadler, N. MacLeod, Q. Cheng, X. Hou, J. Yang, X. Wang, Y. Wang, H. Zhang, X. Chen, G. Li, Y. Zhang, Y. Shi, D. Yuan, Q. Chen, L. Zhang, C. Li, Y. Zhao, A high-resolution summary of Cambrian to Early Triassic marine invertebrate biodiversity. Science. 367, 272-277 (2020).

60. M. Green, D. Hadley-Pryce, C. Scotese, A journey through tides: Phanerozoic (541 Ma-present day). 157-184 (2023).

Figures and Tables

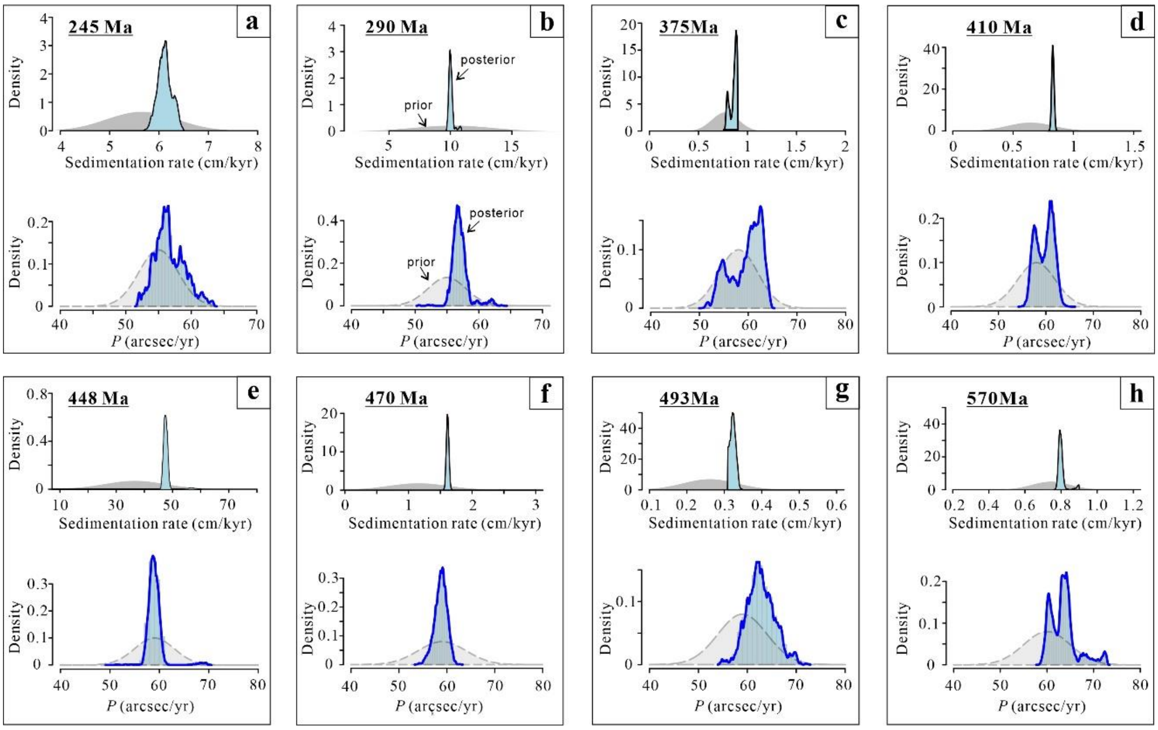

Figure 1. Prior and posterior distributions of the SR and *p*. (a). The cyclostratigraphic record from ref. (37) at 245 Ma and the TimeOptMMC analysis reveals a prominent SR of 6.12±0.14 cm/kyr, while the distribution of *p* values is at 56.70±2.26 arcsec/yr. (b). The cyclostratigraphic record obtained from ref. (32) at 290 Ma indicates a notable SR of 10.04±0.20 cm/kyr, as revealed by the TimeOptMMC analysis. Additionally, the distribution of *p* values is observed to be at 57.06±1.36 arcsec/yr. (c). The cyclostratigraphic record from ref. (38) at 375 Ma reveals a significant SR of 0.81±0.04 cm/kyr, and the distribution of *p* values is observed to be 59.53±3.24 arcsec/yr. (d). The cyclostratigraphic record from ref. (39) at 410 Ma reveals a significant SR of 0.83±0.01 cm/kyr, and the distribution of *p* values is observed to be 59.72±1.89 arcsec/yr. €. The cyclostratigraphic record from ref. (40) at 448 Ma reveals a significant SR of 47.74±1.51 cm/kyr, and the distribution of *p* values is observed to be 59.02±1.63 arcsec/yr. (f). The cyclostratigraphic record from ref. (41) at 470 Ma reveals a significant SR of 1.61±0.02 cm/kyr, and the distribution of *p* values is observed to be 59.21±1.29 arcsec/yr. (g). The cyclostratigraphic record obtained from ref. (42) at 493 Ma reveals a significant SR of 0.34±0.008 cm/kyr, as determined by the TimeOptMMC analysis. Furthermore, the distribution of *p* values is observed to be at 62.76±2.81 arcsec/yr. (h). The cyclostratigraphic record from ref. (43) at 570 Ma and the TimeOptMMC analysis reveals a prominent SR of 0.80±0.02 cm/kyr, while the distribution of *p* values is at 63.49±2.92 arcsec/yr. Shaded grey areas indicate the prior distributions, and blue-shaded histograms indicate the posterior distributions obtained by the Markov Chain Monte Carlo sampling.

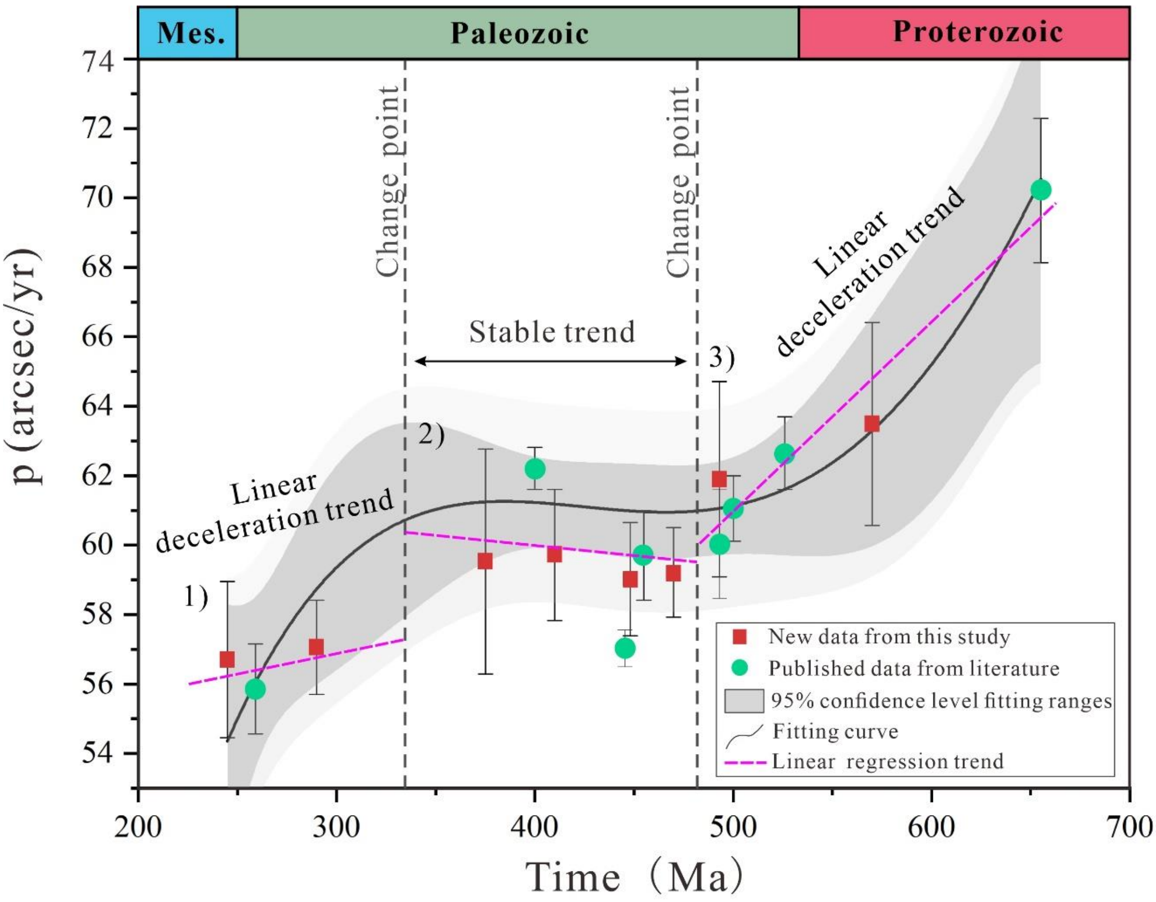

Figure 2. The cyclostratigraphic-reconstructed Earth's precession frequencies and their trends. The grey shaded area indicates the 95% confidence level for the fitted data range. The black curve represents the polynomial fitting results for these data. The black dotted lines represent the outputs of the change-point analysis, which have divided the data into three groups. The purple dotted curves represent the linear regression trends for the data points within each of the three groups. Mes: Mesozoic.

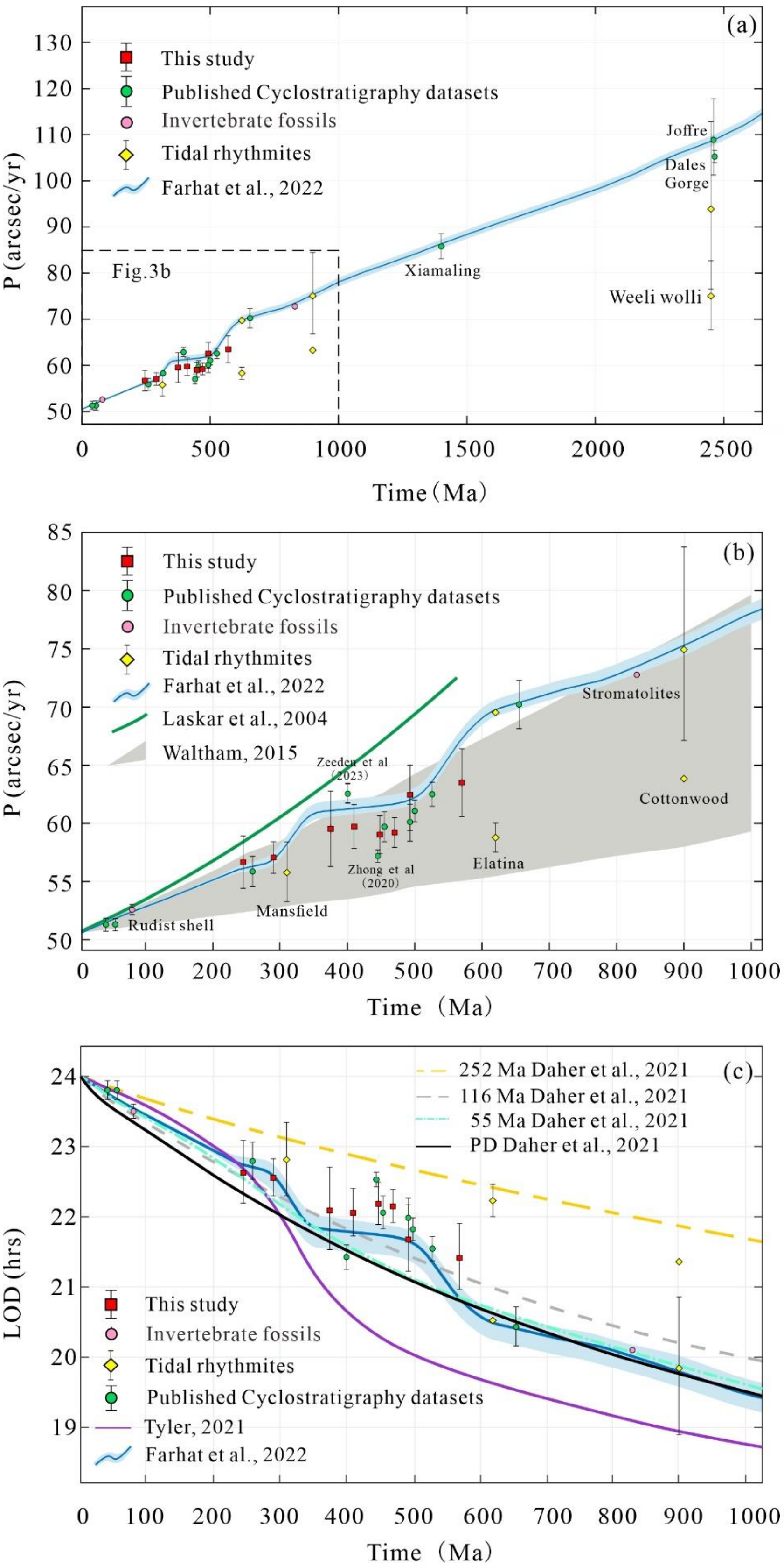

Figure 3. Comparison of *p, LOD* with tidal model predictions. (a). The estimated Earth precession frequency versus the F22 tidal model (16). (b). The estimated Earth precession

frequency versus the astronomical models, the green line shows Laskar's model (Eq (40) in ref. (6)), the blue curve with narrow error range was cited from ref. (16), the grey area delineates the error range given by Waltham's model (13). (c). Comparison of the reconstructed LOD with tidal model results, the tidal models are from the refs. (14-16). Note: the D21 model (14) has calculated four tidal evolution solutions based on present-day (PD) ocean basin geometry and with 55 Ma, 116 Ma, and 252 Ma reconstructed basin paleogeometries. The red square points with error bars are results in this study, the green circle points with error bars data are from published cyclostratigraphic articles, the purple and yellow data points originated from the invertebrate fossils and tidal rhythmites, respectively.

Table 1. The TimeOptMCMC reconstruction results of the cyclostratigraphic records in this study.

Time (Ma)	*p* (arcsec/yr)	EMD (1000 km)	LOD (hrs)	Obliquity (°)
245	56.70±2.26	373.99 (+3.36/-3.22)	22.63 (+0.46/-0.45)	22.62 (+0.21/-0.21)
290	57.06±1.36	373.47 (+1.99/-1.95)	22.55 (+0.28/-0.26)	22.58 (+0.13/-0.12)
375	59.53±3.24	369.96 (+4.63/-4.39)	22.09 (+0.62/-0.56)	22.36 (+0.29/-0.27)
410	59.72±1.89	369.69 (+2.67/-2.58)	22.05 (+0.36/-0.33)	22.35 (+0.16/-0.16)
448	59.02±1.63	370.67 (+2.32/-2.26)	22.18 (+0.31/-0.29)	22.41 (+0.14/-0.14)
470	59.21±1.29	370.40 (+1.83/-1.78)	22.15 (+0.24/-0.23)	22.39 (+0.11/-0.11)
493	62.76±2.81	365.58 (+3.79/-3.63)	21.53 (+0.48/-0.44)	22.16 (+0.24/-0.22)
570	63.49±2.92	364.62 (+3.90/-3.73)	21.41 (+0.49/-0.45)	22.04 (+0.23/-0.23)

Note: EMD represents the Earth-Moon distance; LOD indicates the length of the solar day. The uncertainty of these values are based on 1δ standard deviation.

Supporting Information for:

Geological evidence confirms the staircase patterns of Earth's rotation deceleration from the Neoproterozoic to the Mesozoic Era

He Huang[1,2,3], Chao Ma[1,2,*], Matthias Sinnesael[3], Mohammad Farhat[3], Nam H. Hoang[3], Yuan Gao[4], Christian Zeeden[5], Hanting Zhong[1,2], Mingcai Hou[1,2], Chengshan Wang[4], Jacques Laskar[3]

[1] State Key Laboratory of Oil and Gas Reservoir Geology and Exploitation, Institute of Sedimentary Geology, Chengdu University of Technology, Chengdu 610059, China

[2] Key Laboratory of Deep-time Geography and Environment Reconstruction and Applications of Ministry of Natural Resources, Chengdu University of Technology, Chengdu 610059, China

[3] IMCCE, CNRS, Observatoire de Paris, PSL University, Sorbonne Université, 75014, Paris, France

[4] State Key Laboratory of Biogeology and Environmental Geology, China University of Geosciences (Beijing), Beijing 100083, China

[5] LIAG-Leibniz Institute for Applied Geophysics, Stilleweg 2, 30655 Hannover, Germany

Corresponding author: Chao Ma

Email: machao@cdut.edu.cn

This PDF file includes:

Tables S1 to S2

Figures S1 to S12

Supplementary R scripts

SI References

The paper is a non-peer reviewed preprint submitted to EarthArXiv

Supplementary Tables

Table S1. The detailed information of the geological data in this study. We also provided some of the key parameters for running the TimeOpt and TimeOptMCMC analysis.

Epoch/Era	Time (Ma)	Formation /Location/ Fossil	Proxy	TimeOpt r^2_{opt} value	TimeOptMCMC Num. of samples and chains	P (arcsec/yr)	±σ (arcsec/yr)	Data Resource
Today*	0 Ma					50.475838		ref. (6)
Eocene§	41 Ma	Newfoundland Ridge	Ca/Fe			51.28	0.56	ref. (35)
Eocene§	55 Ma	Walvis Ridge	a*(red/green)	0.212	200,000; 150	51.28	0.52	ref. (29)
Campanian†	80 Ma	Rudist Shell	XRF			52.58	0.44	ref. (22)
Anisian	**245 Ma**	**Guandao**	**GR**	**0.207**	**200,000; 100**	**56.70**	**2.26**	**ref. (37)**
Wuchiapingian§	259 Ma	Wujiaping	ARM	0.246	600,000; 50	55.86	1.30	ref. (34)
Artinskian	**290 Ma**	**Lucaogou**	**GR**	**0.199**	**100,000; 150**	**57.06**	**1.36**	**ref. (32)**
Frasnian	**375 Ma**	**H-32, Iowa**	**MS**	**0.19**	**100,000; 200**	**59.53**	**3.24**	**ref. (38)**
Emsian§	~400 Ma		MS			62.61	0.60	ref. (31)
Pragian	**410 Ma**	**Požár-CS**	**MS**	**0.162**	**200,000; 150**	**59.72**	**1.89**	**ref. (39)**
Katian	**448 Ma**	**Anticosti Island**	**K%**	**0.215**	**200,000; 100**	**59.02**	**1.63**	**ref. (40)**
Sandbian§	455 Ma	Pingliang	MS	0.094	1,000,000; 30	59.71	1.29	ref. (34)
Floian	**470 Ma**	**Liangjiashan**	**Ca%**	**0.121**	**600,000; 50**	**59.21**	**1.29**	**ref. (41)**
Jiangshanian	**493 Ma**	**Alum Shale**	**S%**	**0.184**	**200,000; 100**	**62.76**	**2.81**	**ref. (42)**
Cambrian§	500 Ma	Luoyixi section	MS			61.06	0.94	ref. (64)
Cambrian§	526 Ma	Qiongzhusi	Fe/Al			62.65	1.04	ref. (33)
Ediacaran	**570 Ma**	**Doushantuo**	**MS**	**0.189**	**200,000; 100**	**63.49**	**2.92**	**ref. (43)**
Cryogenian§	655 Ma	Datangpo	MS	0.215	1,000,000; 30	70.21	2.08	ref. (34)
Tonian†	830 Ma	Stromatolites				72.77	/	ref. (21)
Tonian†	900 Ma	Tidal laminae				74.9	+8.85/-7.78	ref. (17)

Mesoproterozoic[§]	1400 Ma	Xiamaling	Cu/Al	0.3	1,000,000; 50	85.79	1.36	ref. (29)
Paleoproterozoic[§]	2460 Ma	Joffre	Lithological index			108.6	8.5	ref. (30)
Paleoproterozoic[§]	2465 Ma	Dales Gorge	Greyscale	0.087	1,000,000; 30	105.26	1.35	ref. (34)

[*]Earth's rotation rate estimates from ref. (6).

[§]Earth's rotation results inferred from cyclostratigraphic analysis from the published articles.

[†]Earth's rotation results calculated from the tidalites and/or invertebrate fossil growth cycle from the published articles.

Note: All the errors in this table are one standard deviation (±σ), the bold terms in this table are calculated by this study.

GR: gamma ray; ARM: anhysteretic remanent magnetization; MS: magnetic susceptibility.

Table S2. Definition of TimeOptMCMC priors for sedimentation rate, Earth axial precession frequency *p* and secular frequency g_i terms.

Time (Ma)	Sedimentary rate (cm/kyr)	*P* (arcsec/yr)	g_i terms (arcsec/yr)
245	4-7 (ref. 37)	54.5 ± 2.5	
290	2-18 (ref. 32)	55 ± 3	$g_1=5.525 \pm 0.125$
375	0.7-1 (ref. 38)	58 ± 4	$g_2=7.455 \pm 0.015$
410	0.2-1(ref. 39)	58 ± 4	$g_3=17.3 \pm 0.15$
448	10-60 (ref. 40)	59 ± 4	$g_4=17.85 \pm 0.15$
470	0.1-1.8 (ref. 41)	59 ± 5	$g_5=4.257455 \pm 0.00002$
493	0.1-0.4 (ref.42)	59 ± 5	
570	0.5-0.9 (ref.43)	60 ± 5	

Note: Prior distributions for the fundamental frequencies g_1 to g_5 are based on the full range of variability in the model simulations of ref. (6) computed over 500 My. The prior distribution for the precession frequency is derived from the recent study by ref. (13).

Supplementary Figures

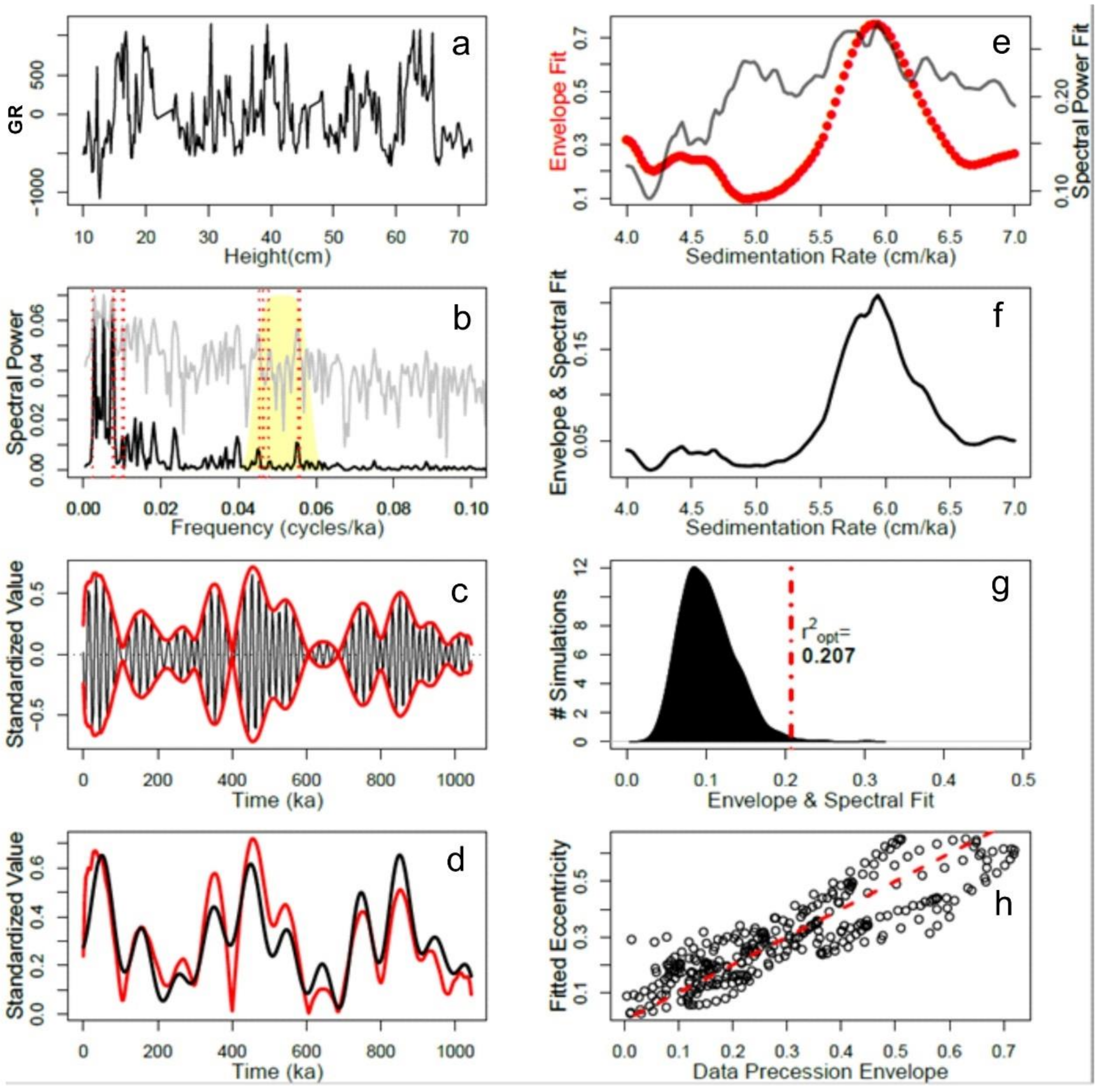

Figure S1. TimeOpt analysis of the GR data from the Guandao section. (a) The GR data of Guandao section (37). (b) Periodogram for the GR data (black line=linear spectrum; gray line=log spectrum). Yellow shaded region indicates the portion of the spectrum bandpass filtered for evaluation of the precession amplitude envelope. Vertical dashed red lines indicate the eccentricity and climatic precession target periods. (c) Extracting the band-passed precession signal (black), and the data amplitude envelope (red) determined via Hilbert transform. (d) Comparison of the data amplitude envelope (red) and the TimeOpt reconstructed eccentricity model (black). (e) Squared Pearson correlation coefficient for the amplitude envelope fit and the spectral power fit as a function of sedimentation rate. (f) Combined envelope and spectral power fit at each evaluated sedimentation rate. (g) Summary of 2000 Monte Carlo simulations with AR1 surrogates. (h) Cross plot of the data amplitude envelope and the TimeOpt-reconstructed eccentricity model in panel "d"; dashed red line is the 1:1 line.

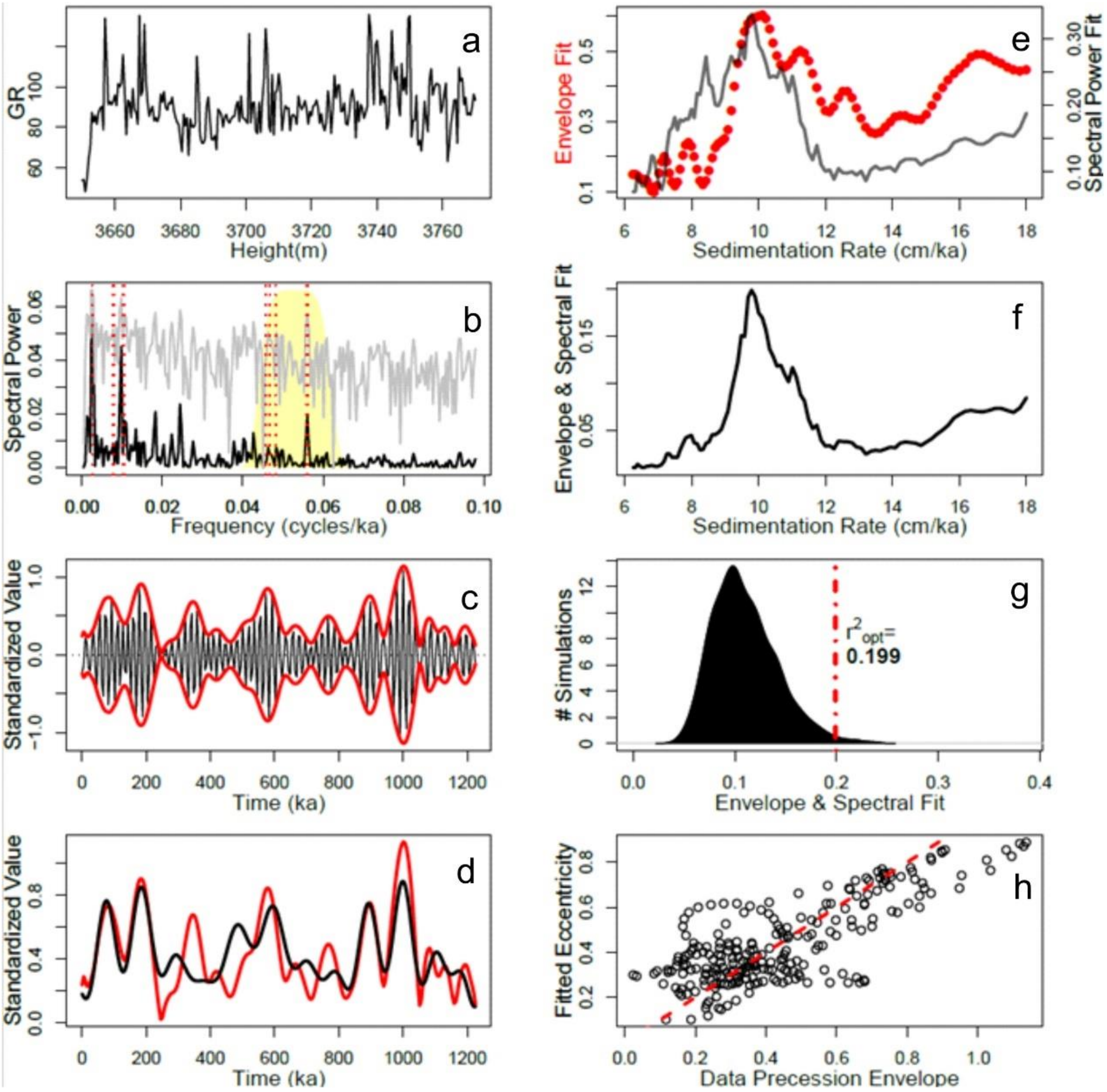

Figure S2. TimeOpt analysis of the GR series from the Lucaogou Formation. (a) The GR data of Ji251 well (32), which geological age was recalibrated by ref. (61). (b) Periodogram for the GR data, given the TimeOpt derived sedimentation rate of 9-10 cm/kyr (black line=linear spectrum; gray line=log spectrum). Yellow shaded region indicates the portion of the spectrum bandpassed for evaluation of the precession amplitude envelope. Vertical dashed red line indicate the eccentricity and climatic precession target periods. (c) Extracting the band-passed precession signal (black), and the data amplitude envelope (red) determined via Hilbert transform. (d) Comparison of the data amplitude envelope (red) and the TimeOpt reconstructed eccentricity model (black). (e) Squared Pearson correlation coefficient for the amplitude envelope fit and the spectral power fit as a function of sedimentation rate. (f) Combined envelope and spectral power fit at each evaluated sedimentation rate. (g) Summary of 2000 Monte Carlo simulations with AR1 surrogates. (h) Cross plot of the data amplitude envelope and the TimeOpt-reconstructed eccentricity model in panel “d”; dashed red line is the 1:1 line.

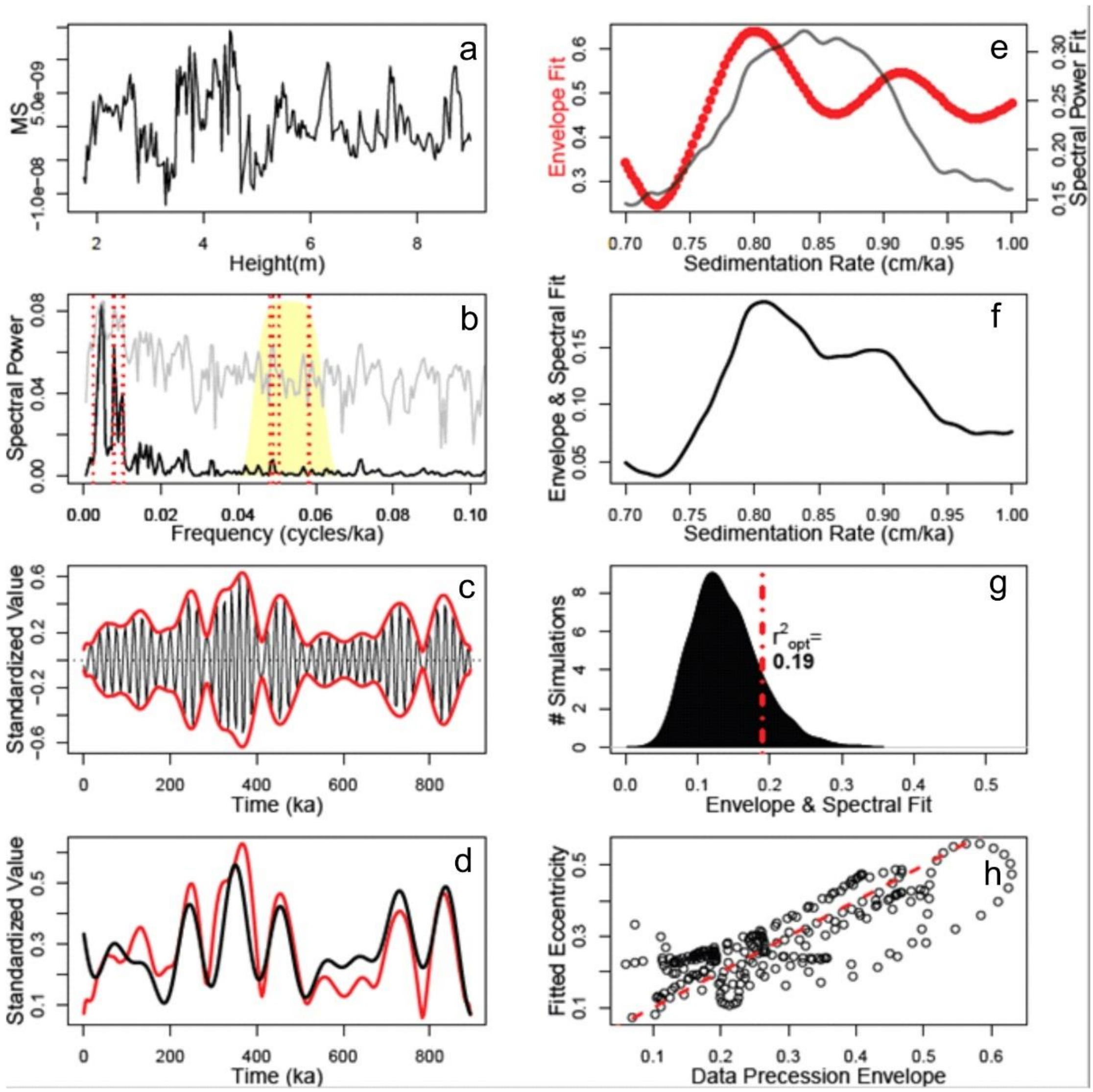

Figure S3. TimeOpt analysis of the MS series from the H-32 core. (a) The MS data of H-32 core (38). (b) Periodogram for the MS data (black line=linear spectrum; gray line=log spectrum). Yellow shaded region indicates the portion of the spectrum bandpassed for evaluation of the precession amplitude envelope. Vertical dashed red line indicate the eccentricity and climatic precession target periods. (c) Extracting the band-passed precession signal (black), and the data amplitude envelope (red) determined via Hilbert transform. (d) Comparison of the data amplitude envelope (red) and the TimeOpt reconstructed eccentricity model (black). (e) Squared Pearson correlation coefficient for the amplitude envelope fit and the spectral power fit as a function of sedimentation rate. (f) Combined envelope and spectral power fit at each evaluated sedimentation rate. (g) Summary of 2000 Monte Carlo simulations with AR1 surrogates. (h) Cross plot of the data amplitude envelope and the TimeOpt-reconstructed eccentricity model in panel “d”; dashed red line is the 1:1 line.

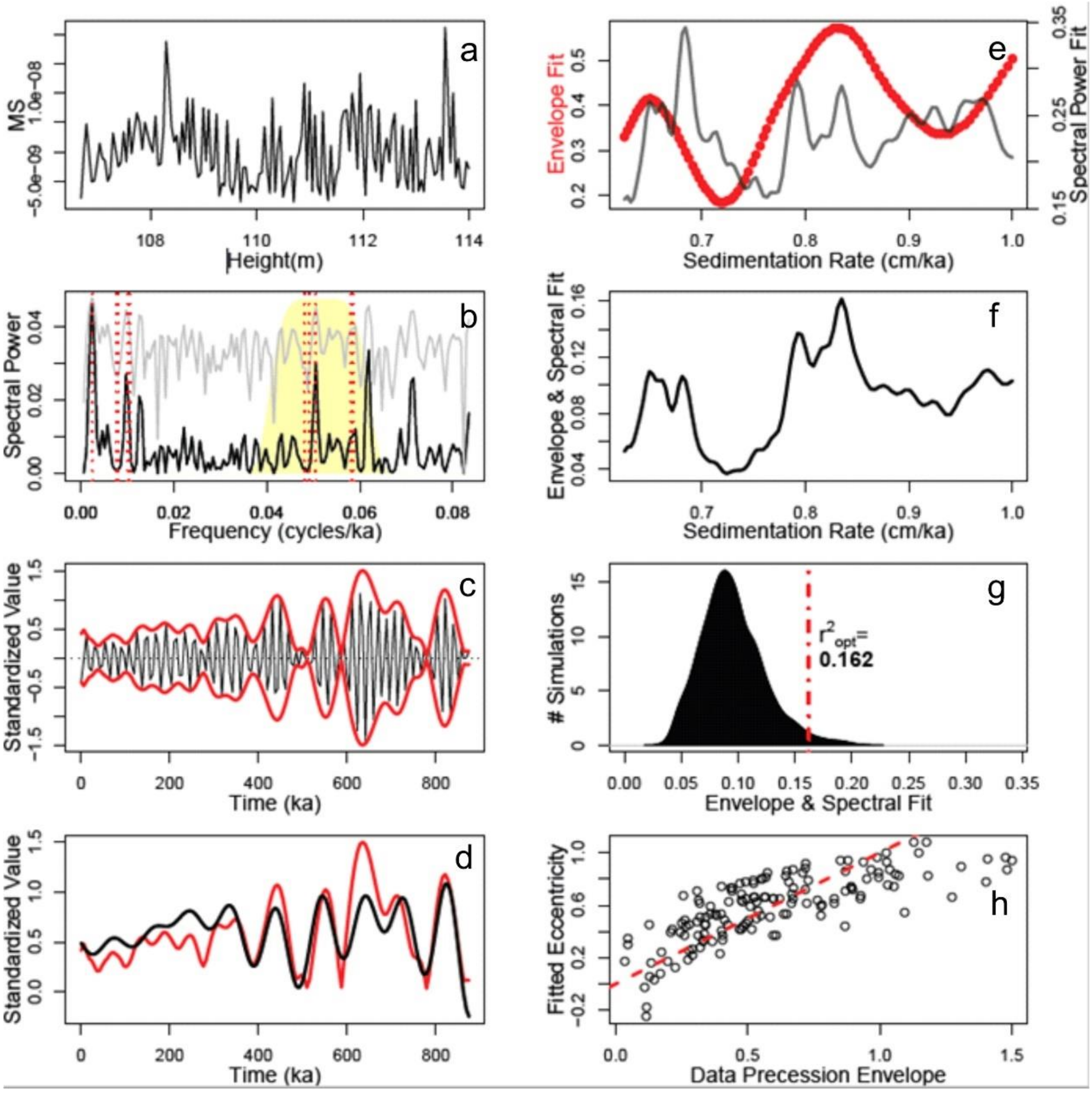

Figure S4. TimeOpt analysis of the MS series from the Požár-CS section. (a) The MS data of the Požár-CS section (39). (b) Periodogram for the MS data (black line=linear spectrum; gray line=log spectrum). Yellow shaded region indicates the portion of the spectrum bandpassed for evaluation of the precession amplitude envelope. Vertical dashed red line indicate the eccentricity and climatic precession target periods. (c) Extracting the band-passed precession signal (black), and the data amplitude envelope (red) determined via Hilbert transform. (d) Comparison of the data amplitude envelope (red) and the TimeOpt reconstructed eccentricity model (black). (e) Squared Pearson correlation coefficient for the amplitude envelope fit and the spectral power fit as a function of sedimentation rate. (f) Combined envelope and spectral power fit at each evaluated sedimentation rate. (g) Summary of 2000 Monte Carlo simulations with AR1 surrogates. (h) Cross plot of the data amplitude envelope and the TimeOpt-reconstructed eccentricity model in panel “d”; dashed red line is the 1:1 line.

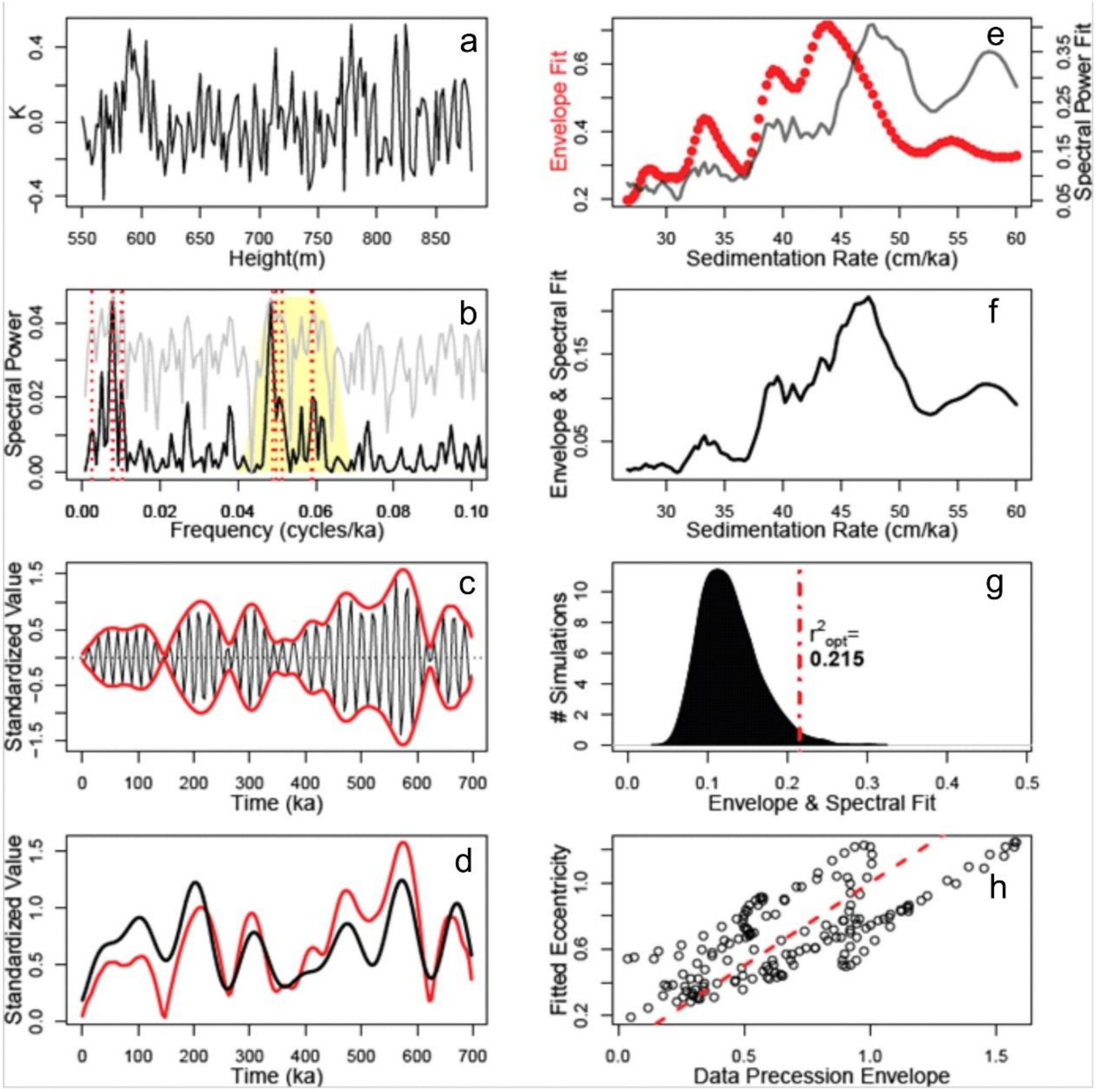

Figure S5. TimeOpt analysis of the K% series from the Upper Ordovician reference section in Anticosti Island, Canada. (a) The K data of the Upper Ordovician reference section (40). (b) Periodogram for the K data (black line=linear spectrum; gray line=log spectrum). Yellow shaded region indicates the portion of the spectrum bandpassed for evaluation of the precession amplitude envelope. Vertical dashed red line indicate the eccentricity and climatic precession target periods. (c) Extracting the band-passed precession signal (black), and the data amplitude envelope (red) determined via Hilbert transform. (d) Comparison of the data amplitude envelope (red) and the TimeOpt reconstructed eccentricity model (black). (e) Squared Pearson correlation coefficient for the amplitude envelope fit and the spectral power fit as a function of sedimentation rate. (f) Combined envelope and spectral power fit at each evaluated sedimentation rate. (g) Summary of 2000 Monte Carlo simulations with AR1 surrogates. (h) Cross plot of the data amplitude envelope and the TimeOpt-reconstructed eccentricity model in panel “d”; dashed red line is the 1:1 line.

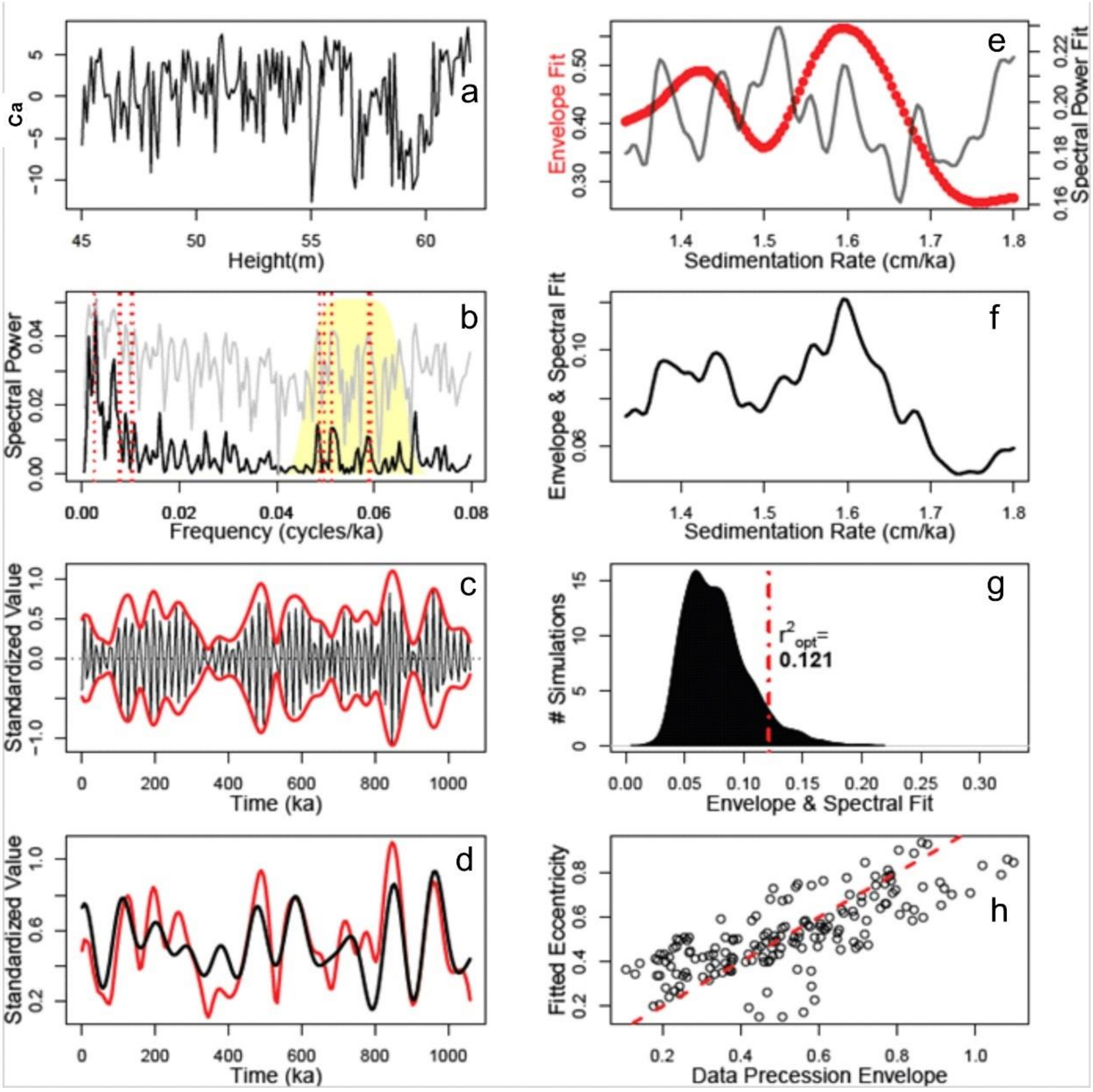

Figure S6. TimeOpt analysis of the Ca% series from the Liangjiashan section. (a) The Ca% data of the Liangjiashan section (41). (b) Periodogram for the Ca% data (black line=linear spectrum; gray line=log spectrum). Yellow shaded region indicates the portion of the spectrum bandpassed for evaluation of the precession amplitude envelope. Vertical dashed red line indicate the eccentricity and climatic precession target periods. (c) Extracting the band-passed precession signal (black), and the data amplitude envelope (red) determined via Hilbert transform. (d) Comparison of the data amplitude envelope (red) and the TimeOpt reconstructed eccentricity model (black). (e) Squared Pearson correlation coefficient for the amplitude envelope fit and the spectral power fit as a function of sedimentation rate. (f) Combined envelope and spectral power fit at each evaluated sedimentation rate. (g) Summary of 2000 Monte Carlo simulations with AR1 surrogates. (h) Cross plot of the data amplitude envelope and the TimeOpt-reconstructed eccentricity model in panel “d”; dashed red line is the 1:1 line.

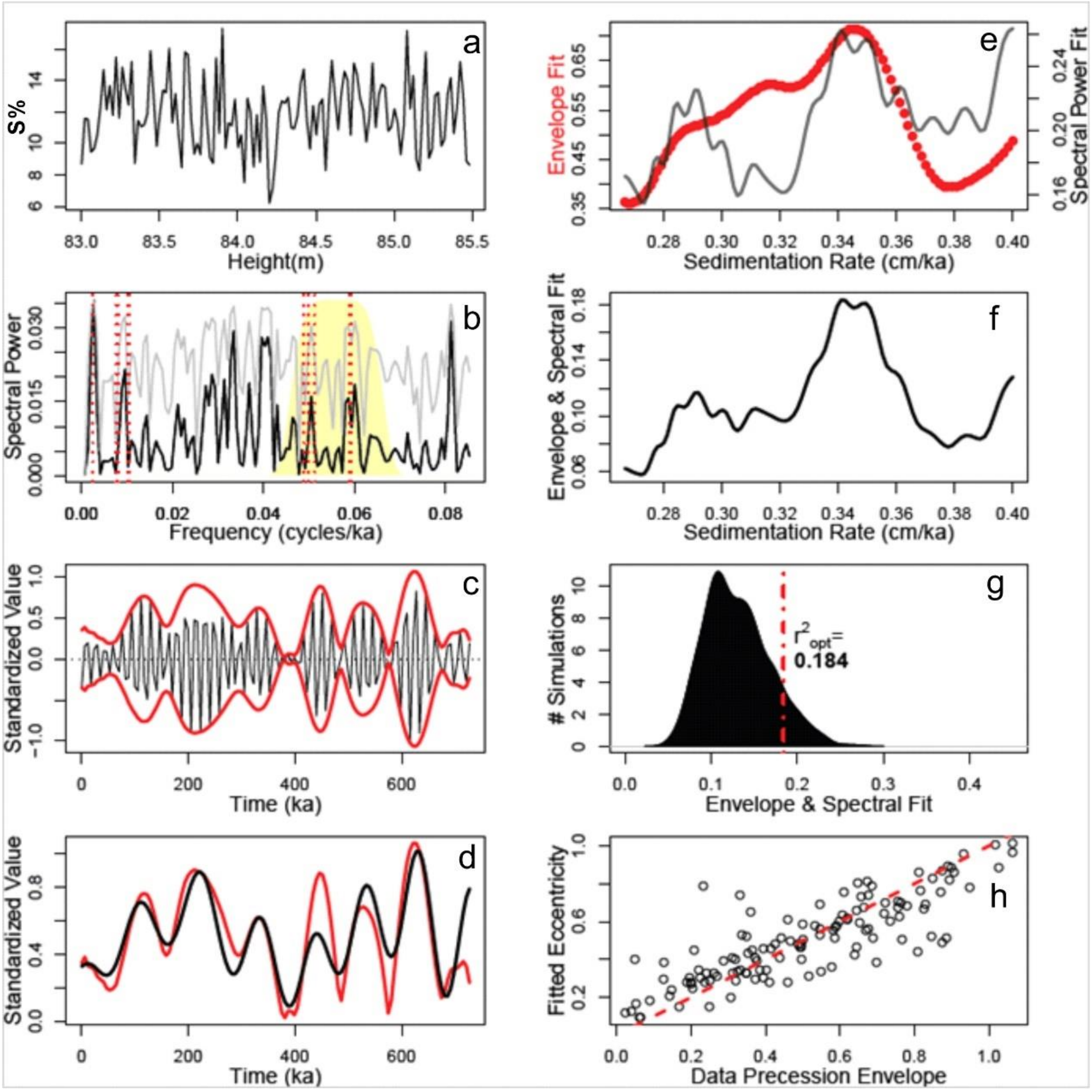

Figure S7. TimeOpt analysis of the S% series from the Alum Shale Formation. (a) The S% data of the Alum Shale (42). (b) Periodogram for the S% data (black line=linear spectrum; gray line=log spectrum). Yellow shaded region indicates the portion of the spectrum bandpassed for evaluation of the precession amplitude envelope. Vertical dashed red line indicate the eccentricity and climatic precession target periods. (c) Extracting the band-passed precession signal (black), and the data amplitude envelope (red) determined via Hilbert transform. (d) Comparison of the data amplitude envelope (red) and the TimeOpt reconstructed eccentricity model (black). (e) Squared Pearson correlation coefficient for the amplitude envelope fit and the spectral power fit as a function of sedimentation rate. (f) Combined envelope and spectral power fit at each evaluated sedimentation rate. (g) Summary of 2000 Monte Carlo simulations with AR1 surrogates. (h) Cross plot of the data amplitude envelope and the TimeOpt-reconstructed eccentricity model in panel "d"; dashed red line is the 1:1 line.

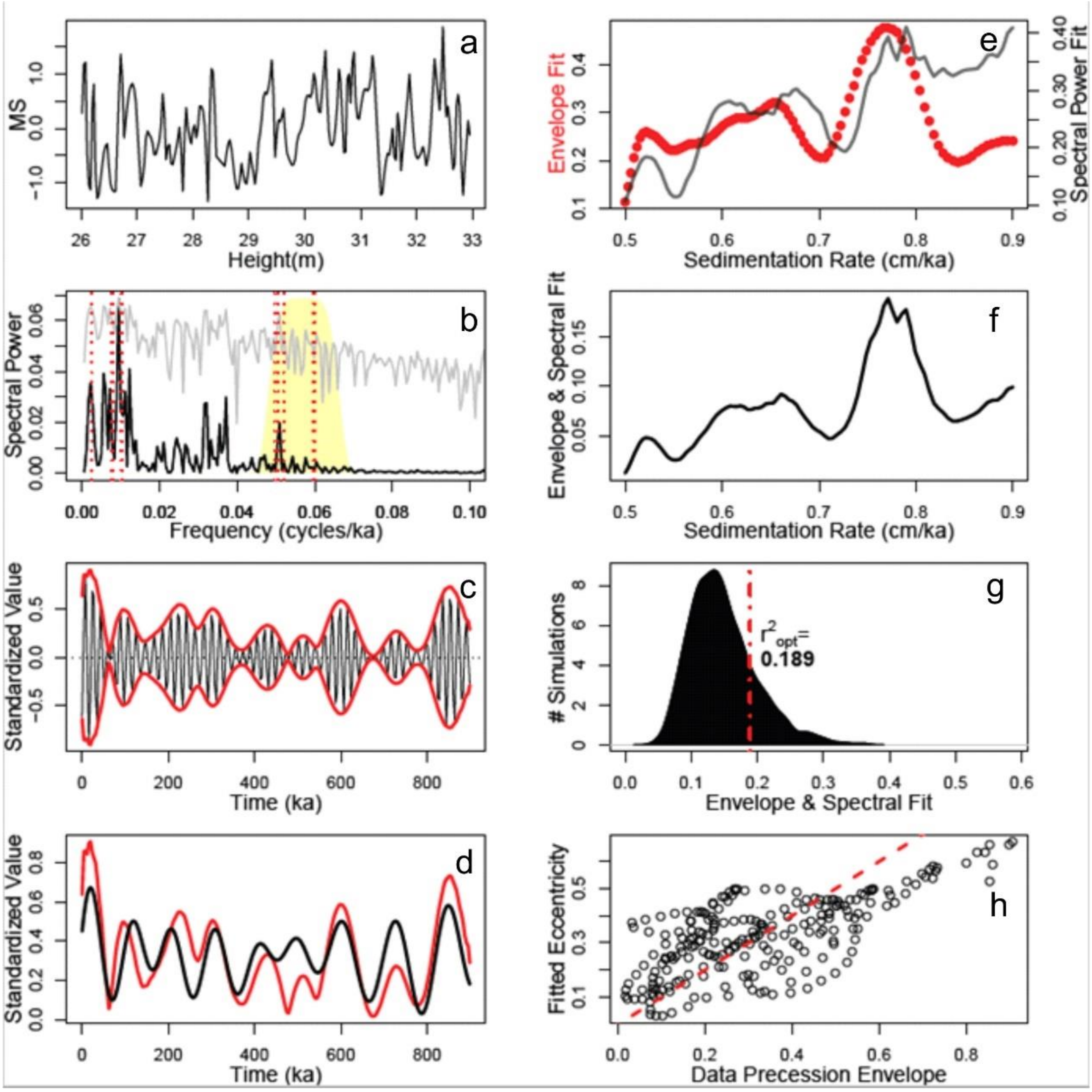

Figure S8. TimeOpt analysis of the MS series from the Doushantuo Formation. (a) The MS data of the Doushantuo Formation (43). (b) Periodogram for the MS data (black line=linear spectrum; gray line=log spectrum). Yellow shaded region indicates the portion of the spectrum bandpassed for evaluation of the precession amplitude envelope. Vertical dashed red line indicate the eccentricity and climatic precession target periods. (c) Extracting the band-passed precession signal (black), and the data amplitude envelope (red) determined via Hilbert transform. (d) Comparison of the data amplitude envelope (red) and the TimeOpt reconstructed eccentricity model (black). (e) Squared Pearson correlation coefficient for the amplitude envelope fit and the spectral power fit as a function of sedimentation rate. (f) Combined envelope and spectral power fit at each evaluated sedimentation rate. (g) Summary of 2000 Monte Carlo simulations with AR1 surrogates. (h) Cross plot of the data amplitude envelope and the TimeOpt-reconstructed eccentricity model in panel "d"; dashed red line is the 1:1 line.

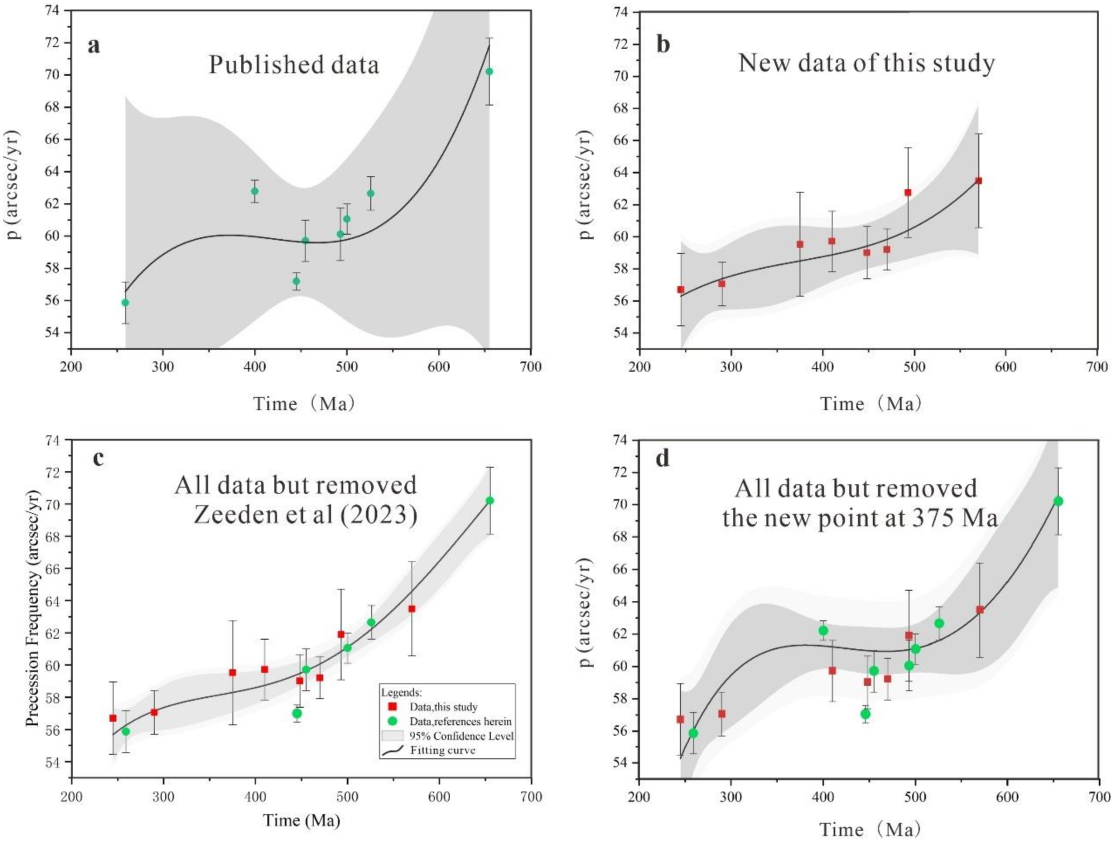

Figure S9. Fitting the reconstructed precession frequencies from 200 Ma to 700 Ma. (a) The fitting curve of the published data is derived from the cubic polynomial fitting. Evidently, there are a wide range of possibility of the fitting result. (b) The new data is also used the cubic polynomial fitting to find out their trends and variations. (c) Fitting all of the data but except the data from Zeeden et al. (2023). (d) After removing the data point at 375 Ma, we have fitted the rest of data by using the quartic polynomial fitting approach, the fitting curve has shown a clearly staircase pattern.

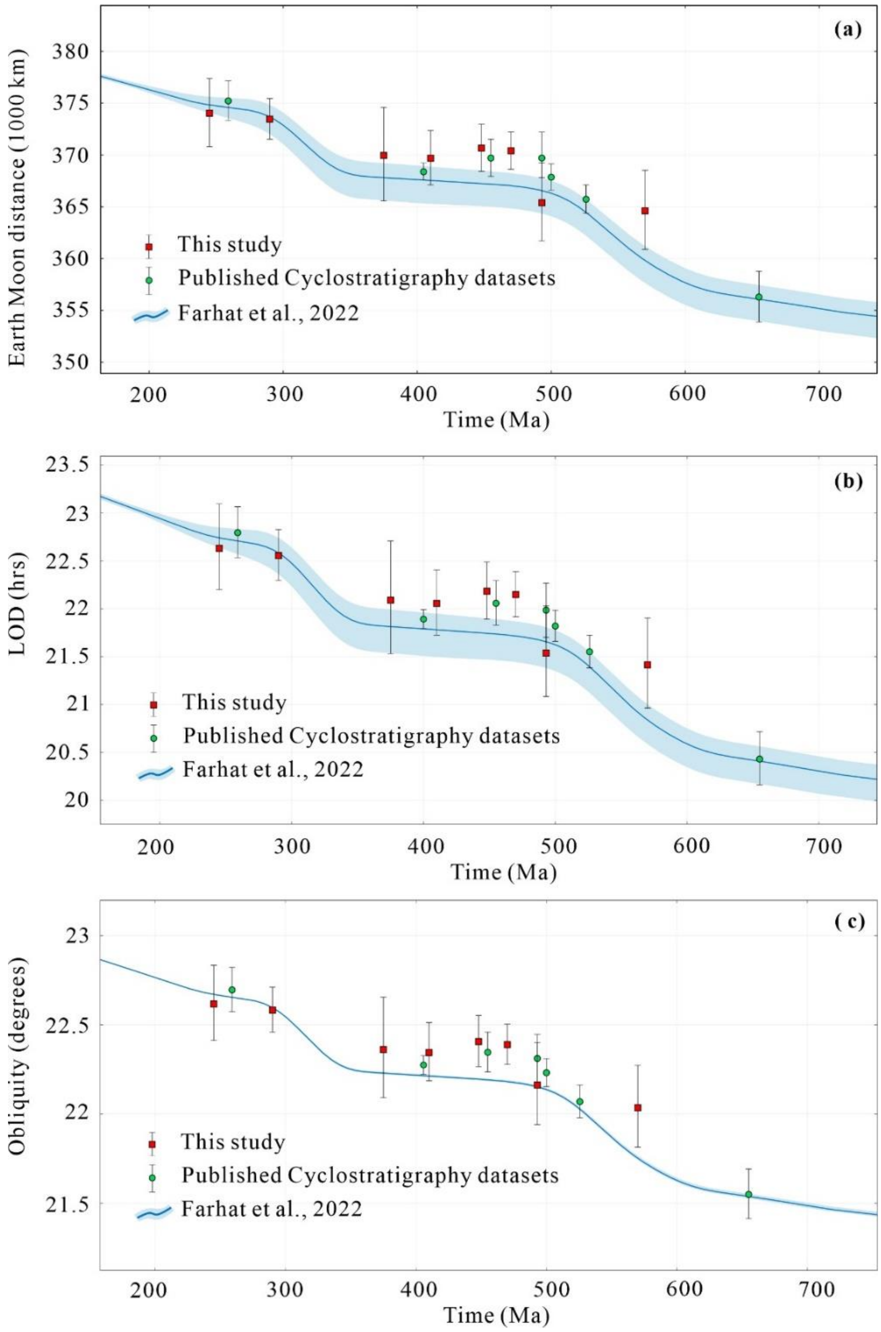

Figure S10. Reconstruction of the (a) Earth-Moon distance (EMD), (b) length of solar day (LOD) and (c) obliquity degrees based on the Earth's precession frequency (*p*) results originated from the TimeOptMCMC analysis. The red square dots are calculated from this study, while the green circle dots are compiled from the published research articles (reference herein). The EMD, LOD and obliquity degrees were obtained from the *AstroGeo22* tool on the *AsotroGeo* website (http://www.astrogeo.eu/).

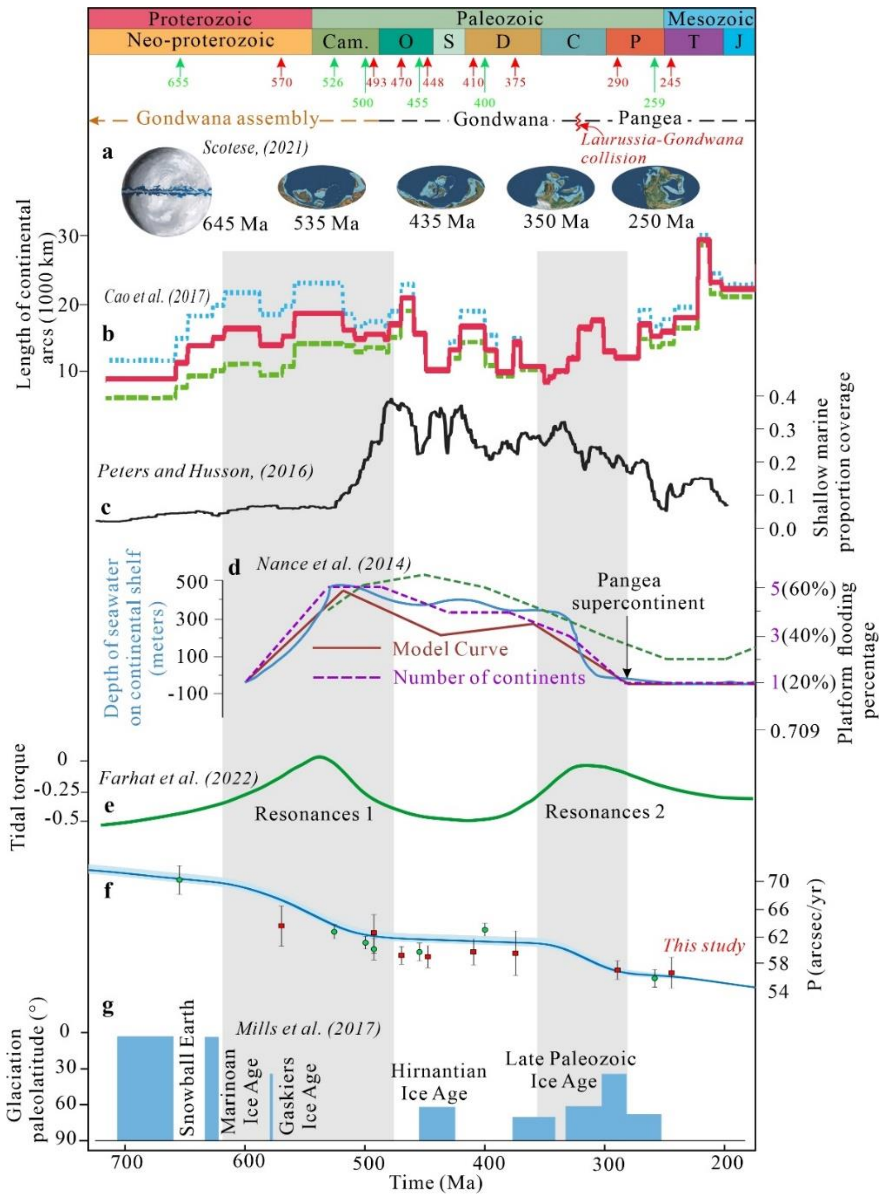

Figure. S11. Correlation between the Earth's rotation rate and the trends of multiple tectonic and environmental records. (a). The paleogeographic maps of Earth (62). (b). Continental arc length in the past 750 Ma (49). Dotted blue, dashed green, and solid red curves are the maximum, minimum, and average length estimates, respectively. (c). The shallow marine proportion coverage curve (50). (d). The depth of seawater on continental shelf, the degree of platform flooding and the number of continents from the past ~600 Ma to ~190 Ma (51). (e). The simulated tidal torque and normalized its absolute strength to present value (16). (f). The estimated Earth's precession frequency from geological archives, the blue curve represents the F22 tidal model (16). (g). Paleolatitude of glaciations throughout the Neoproterozoic to Paleozoic (63).

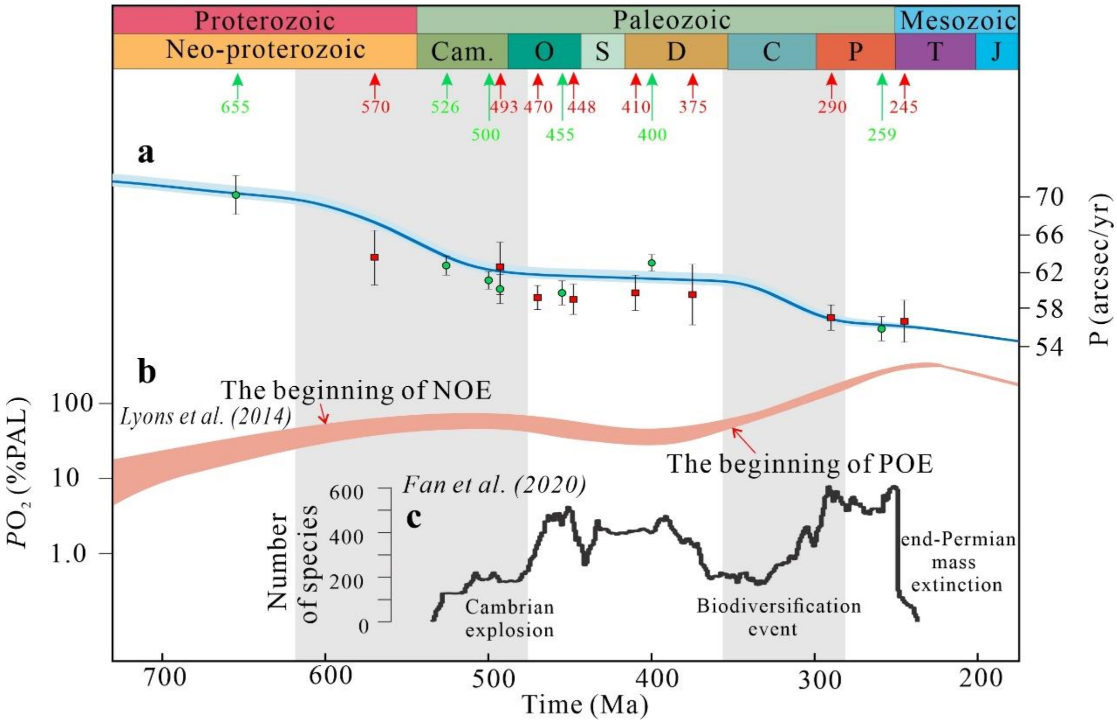

Figure. S12. Correlation between the Earth's rotation rate and the trends of oxygen concentration and species abundance curves. (a). The estimated Earth's precession frequency from geological archives, the blue curve represents the F22 tidal model (16). (b). The evolution of Earth's atmospheric oxygen content from Neoproterozoic to Mesozoic Eras (58). (c). The species diversity from Cambrian to Triassic (59).

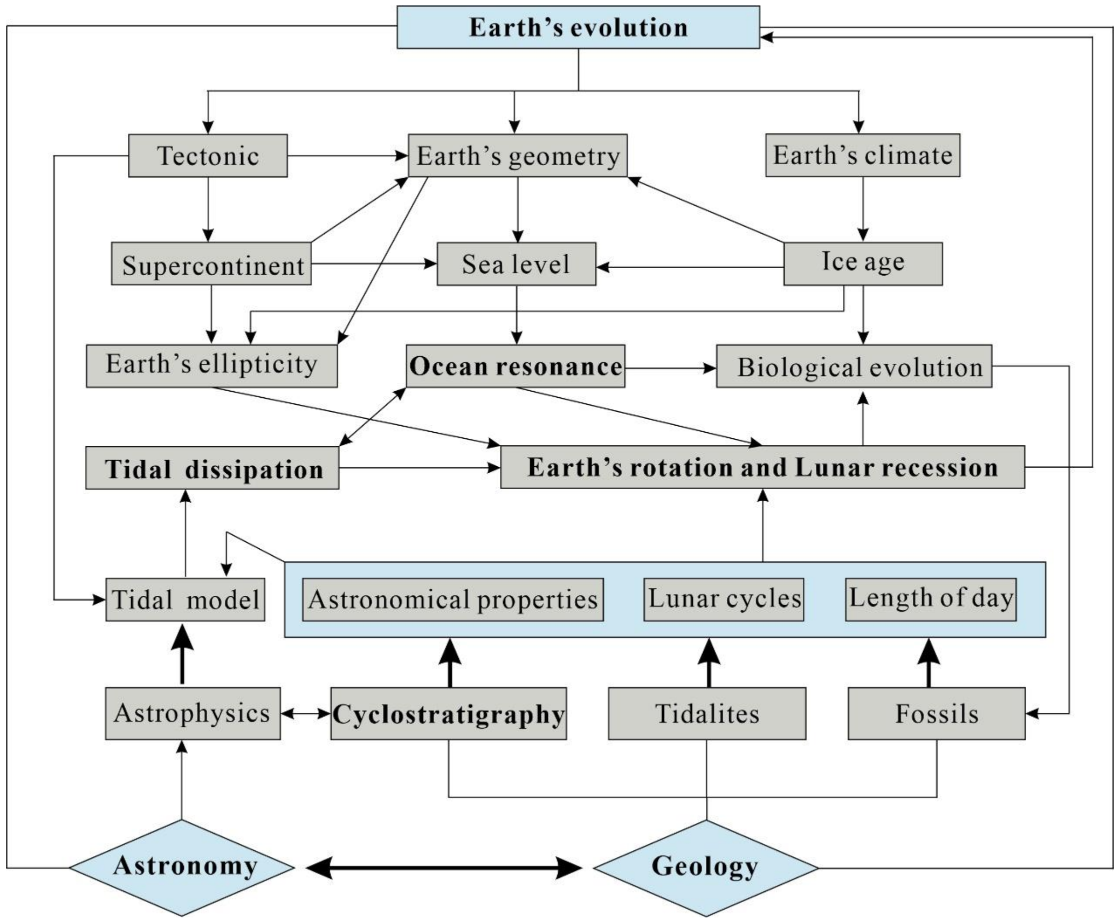

Figure S13. The possible cause-and-effect between the Earth's rotational dynamics and geological processes. In this framework, the variations of the Earth-Moon tidal dissipation and Earth dynamic ellipticity dynamic are two main factors that influence Earth's rotation deceleration. Understanding these connections requires interdisciplinary research combining astrophysics, geophysics, geology, climatology, and other relevant fields. Additionally, international collaborations are necessary to solve these complex issues (e.g., *AstroGeo* project in the Europe and *CycloAstro* project in the U. S).

Supplementary R scripts

The R Scripts for TimeOpt and TimeOptMCMC analysis for this paper

```
##Conduct the TimeOpt and TimtOptMCMC analysis to obtain the precessional constant index (p)
### GR data from Li et al (2018 EPSL), GR series 10-72 m (245 Ma)
library(astrochron)
data=read();
data1=iso(data,xmin=10,xmax=72);
data1=trim(data1,c=2);
data1=noKernel(data1,smooth=0.1);
### Interpolate the data to the median sampling interval
data1=linterp(data1)
###Determine nominal precession and eccentricity periods,then conduct nominal timeOpt analysis
targetTot=calcPeriods(g=c(5.525000,7.455000,17.300000,17.850000,4.257455),k=54.5,output=2);
targetE=sort(targetTot[1:5],decreasing=T);
targetP=sort(targetTot[6:10],decreasing=T);
###run nominal timeOpt and output sedimentation rate grid and fit
res1=timeOpt(data1,sedmin=4,sedmax=7,numsed=100,targetE=targetE,targetP=targetP,flow=1/23,fhigh=1/17,roll=10^7,limit=T,output=1);
###output optimal time series, bandpassed series, amplitude envelope and TimeOpt-reconstructed eccentricity
res2=timeOpt(data1,sedmin=4,sedmax=7,numsed=100,targetE=targetE,targetP=targetP,flow=1/23,fhigh=1/17,roll=10^7,limit=T,output=2);
```

```
###perform nominal timeOpt significance testing
simres=timeOptSim(data1,sedmin=4,sedmax=7,numsed=100,targetE=targetE,targetP=targetP,flow=1/23,fhigh=1/17,roll=10^7,numsim=1000,output=2,ncores=4);
###plot summary figure
timeOptPlot(data1,res1,res2,simres,flow=1/23,fhigh=1/17,fitR=0.20783,roll=10^7,targetE=targetE,targetP=targetP,xlab="Height(cm)",ylab="GR",verbose=T);
###run a single timeOptMCMC chain (100 chains)
res=timeOptMCMC(data1,sedmin=4,sedmax=7,sedstart=5.94,gAve=c(5.525000,7.455000,17.300000,17.850000,4.257455), gSd=c(0.12500,0.01500,0.150005,0.15000,0.00002),gstart=c(-1,-1,-1,-1,-1),kAve=54.5,kSd=2.5,kstart=-1,rhomin=0,rhomax=0.9999,rhostart=1,sigmamin=NULL,sigmamax=NULL,sigmastart=-1,nsamples=200000,
iopt=1,epsilon=c(0.2,0.2,0.35,0.35,0.8,0.85,0.6,0.35,0.9,0.35,0.9)/40,ran=T,burnin=-1,savefile = F);
### output the TimeOptMCMC results
write.table(res,file="Li_GR_TimeOptMCMC_results.csv",sep=",",row.names=FALSE)


###TimeOptMCMC analysis the Ji251 NGR series from Huang et al., 2020_P3 (290Ma)
library(astrochron);
###Obtain the target dataset
ji=read()
ji251=iso(ji,xmin=3650,xmax=3770);
ji1=trim(ji251,c=3);
ji2=linterp(ji1,dt=0.5);
###Determine nominal precession and eccentricity periods,then conduct nominal timeOpt analysis
targetTot=calcPeriods(g=c(5.525000,7.455000,17.300000,17.850000,4.257455),k=55,output=2);
targetE=sort(targetTot[1:5],decreasing=T);
```

```
targetP=sort(targetTot[6:10],decreasing=T);
###run nominal timeOpt and output sedimentation rate grid and fit
res1=timeOpt(ji2,sedmin=2,sedmax=18,numsed=100,targetE=targetE,targetP=targetP,flow=1/23,fhigh=1/16,roll=10^7,limit=T,output=1);
###output optimal time series, bandpassed series, amplitude envelope and TimeOpt-reconstructed eccentricity
res2=timeOpt(ji2,sedmin=2,sedmax=18,numsed=100,targetE=targetE,targetP=targetP,flow=1/23,fhigh=1/16,roll=10^7,limit=T,output=2);
###perform nominal timeOpt significance testing
simres=timeOptSim(ji2,sedmin=2,sedmax=18,numsed=100,targetE=targetE,targetP=targetP,flow=1/23,fhigh=1/16,roll=10^7,numsim=2000,output=2,ncores=6);
###plot summary figure
timeOptPlot(ji2,res1,res2,simres,flow=1/23,fhigh=1/16,fitR=0.19915,roll=10^7,targetE=targetE,targetP=targetP,xlab="Height(m)",ylab="NGR",verbose=T);
###run a single timeOptMCMC chain (150 chain)
res=timeOptMCMC(ji2,sedmin=2,sedmax=18,sedstart=9.78,gAve=c(5.525000,7.455000,17.300000,17.850000,4.257455),gSd=c(0.12500,0.01500,0.150005,0.15000,0.00002),gstart=c(-1,-1,-1,-1,-1),kAve=55,kSd=3,kstart=-1,rhomin=0,rhomax=0.9999,rhostart=-1,sigmamin=NULL,sigmamax=NULL,sigmastart=1,nsamples=100000,iopt=1,epsilon=c(0.2,0.2,0.35,0.35,0.8,0.85,0.6,0.35,0.9,0.35,0.9)/20,ran=T,burnin=-1);
### output the TimeOptMCMC results
write.table(res,file="Huang_NGR_TimeOptMCMC_results.csv",sep=",",row.names=FALSE)


### Data from De Vleeschouwer et al (2017 Nature Communications) H32_MS series, 176-900cm (~375 Ma)
###(1)load the Astrochron package
library(astrochron);
###(2) Obtain the target dataset
data=read();
```

```
data1=iso(data,xmin=176,xmax=900);
# Convert depth from cm to m
data1[1]=data1[1]/100
data1=noKernel(data1,smooth=0.1);
data1=trim(data1,c=1.5);
###(3) Interpolate the data to the median sampling interval
data1=linterp(data1);
###Determine nominal precession and eccentricity periods,then conduct nominal timeOpt analysis
targetTot=calcPeriods(g=c(5.525000,7.455000,17.300000,17.850000,4.257455),k=58,output=2);
targetE=sort(targetTot[1:5],decreasing=T);
targetP=sort(targetTot[6:10],decreasing=T);
###run nominal timeOpt and output sedimentation rate grid and fit
res1=timeOpt(data1,sedmin=0.7,sedmax=1,numsed=100,targetE=targetE,targetP=targetP,flow=1/23,fhigh=1/16,roll=10^7,limit=T,output=1);
###output optimal time series, bandpassed series, amplitude envelope and TimeOpt-reconstructed eccentricity
res2=timeOpt(data1,sedmin=0.7,sedmax=1,numsed=100,targetE=targetE,targetP=targetP,flow=1/23,fhigh=1/16,roll=10^7,limit=T,output=2);
###perform nominal timeOpt significance testing
simres=timeOptSim(data1,sedmin=0.7,sedmax=1,numsed=100,targetE=targetE,targetP=targetP,flow=1/23,fhigh=1/16,roll=10^7,numsim=2000,output=2,ncores=6);
###plot summary figure
timeOptPlot(data1,res1,res2,simres,flow=1/23,fhigh=1/16,fitR=0.18966,roll=10^7,targetE=targetE,targetP=targetP,xlab="Height(m)",ylab="MS",verbose=T);
###run a single timeOptMCMC chain (200 chain)
res=timeOptMCMC(data1,sedmin=0.7,sedmax=1,sedstart=0.83,gAve=c(5.525000,7.455000,17.300000,17.850000,4.257455),gSd=c(0.12500,0.01500,0.150005,0.15000,0.00002),gstart=
```

```
c(-1,-1,-1,-1,-1),kAve=58,kSd=4,kstart=-1,rhomin=0,rhomax=0.9999,rhostart=-1,sigmamin=NULL,sigmamax=NULL,sigmastart=-1,nsamples=100000,
iopt=1,epsilon=c(0.2,0.2,0.35,0.35,0.8,0.85,0.6,0.35,0.9,0.35,0.9)/20,ran=T,burnin=-1);
### output the TimeOptMCMC results
write.table(res,file="David_MS_375Ma_TimeOptMCMC_results.csv",sep=",",row.names=FALSE)

### Data from Da Silva et al (2016 EPSL) Požár-CS section_MS series (106.7-114m), (~410 Ma).
###(1)load the Astrochron package
library(astrochron);
###(2) Obtain the target dataset
data=read();
data1=iso(data,xmin=106.7,xmax=114);
data1=noKernel(data1,smooth=0.5);
data1=trim(data1,c=2);
###(3) Interpolate the data to the median sampling interval
data1=linterp(data1);
###Determine nominal precession and eccentricity periods,then conduct nominal timeOpt analysis
targetTot=calcPeriods(g=c(5.525000,7.455000,17.300000,17.850000,4.257455),k=58,output=2);
targetE=sort(targetTot[1:5],decreasing=T);
targetP=sort(targetTot[6:10],decreasing=T);
###run nominal timeOpt and output sedimentation rate grid and fit
res1=timeOpt(data1,sedmin=0.2,sedmax=1,numsed=100,targetE=targetE,targetP=targetP,flow=1/25,fhigh=1/16,roll=10^7,limit=T,output=1);
```

```
###output optimal time series, bandpassed series, amplitude envelope and TimeOpt-reconstructed eccentricity

res2=timeOpt(data1,sedmin=0.2,sedmax=1,numsed=100,targetE=targetE,targetP=targetP,flow=1/25,fhigh=1/16,roll=10^7,limit=T,output=2);

###perform nominal timeOpt significance testing

simres=timeOptSim(data1,sedmin=0.2,sedmax=1,numsed=100,targetE=targetE,targetP=targetP,flow=1/25,fhigh=1/16,roll=10^7,numsim=2000,output=2,ncores=6);

###plot summary figure

timeOptPlot(data1,res1,res2,simres,flow=1/25,fhigh=1/16,fitR=0.162,roll=10^7,targetE=targetE,targetP=targetP,xlab="Height(m)",ylab="MS",verbose=T);

###run a single timeOptMCMC chain (150 chain)

res=timeOptMCMC(data1,sedmin=0.2,sedmax=1,sedstart=0.83,gAve=c(5.525000,7.455000,
17.300000,17.850000,4.257455),gSd=c(0.12500,0.01500,0.150005,0.15000,0.00002),gstart=
c(-1,-1,-1,-1,-1),kAve=58,kSd=4,kstart=-1,rhomin=0,rhomax=0.9999,rhostart=-1,sigmamin=NULL,sigmamax=NULL,sigmastart=-1,nsamples=200000,

iopt=1,epsilon=c(0.2,0.2,0.35,0.35,0.8,0.85,0.6,0.35,0.9,0.35,0.9)/20,ran=T,burnin=-1);

### output the TimeOptMCMC results

write.table(res,file="Dasilva_MS_410Ma_TimeOptMCMC_results.csv",sep=",",row.names=FALSE)


### Data from Sinnesael et al (2021 Geology) 550-900 m K% time series (~448 Ma)

###(2) Obtain the target dataset

library(astrochron);

data=read()

data1=noKernel(data,smooth=0.1);

data1=iso(data1,xmin=550,xmax=900);

data1=trim(data1,c=1.5);

data2=linterp(data1,dt=2);
```

```
###Determine nominal precession and eccentricity periods,then conduct nominal timeOpt analysis
targetTot=calcPeriods(g=c(5.525000,7.455000,17.300000,17.850000,4.257455),k=59,output=2);
targetE=sort(targetTot[1:5],decreasing=T);
targetP=sort(targetTot[6:10],decreasing=T);
###run nominal timeOpt and output sedimentation rate grid and fit
res1=timeOpt(data2,sedmin=10,sedmax=60,numsed=100,targetE=targetE,targetP=targetP,flow=1/23,fhigh=1/15,roll=10^7,limit=T,output=1);
###output optimal time series, bandpassed series, amplitude envelope and TimeOpt-reconstructed eccentricity
res2=timeOpt(data2,sedmin=10,sedmax=60,numsed=100,targetE=targetE,targetP=targetP,flow=1/23,fhigh=1/15,roll=10^7,limit=T,output=2);
###perform nominal timeOpt significance testing
simres=timeOptSim(data2,sedmin=10,sedmax=60,numsed=100,targetE=targetE,targetP=targetP,flow=1/23,fhigh=1/15,roll=10^7,numsim=2000,output=2,ncores=6);
###plot summary figure
timeOptPlot(data2,res1,res2,simres,flow=1/23,fhigh=1/15,fitR=0.21654,roll=10^7,targetE=targetE,targetP=targetP,xlab="Height(m)",ylab="K",verbose=T);
###run a single timeOptMCMC chain (100 chain)
res=timeOptMCMC(data2,sedmin=10,sedmax=60,sedstart=47.3,gAve=c(5.525000,7.455000,17.300000,17.850000,4.257455),gSd=c(0.12500,0.01500,0.150005,0.15000,0.00002),gstart=c(-1,-1,-1,-1,-1),kAve=59,kSd=4,kstart=-1,rhomin=0,rhomax=0.9999,rhostart=-1,sigmamin=NULL,sigmamax=NULL,sigmastart=1,nsamples=200000,
iopt=1,epsilon=c(0.2,0.2,0.35,0.35,0.8,0.85,0.6,0.35,0.9,0.35,0.9)/20,ran=T,burnin=-1);
### output the TimeOptMCMC results
write.table(res,file="Sinnesael_K_445Ma_TimeOptMCMC_results.csv",sep=",",row.names=FALSE)

### Data from Ma et al (2019 P3) LJS Ca% time series (~470 Ma)
```

```
###(2) Obtain the target dataset
library(astrochron);
data=read()
data1=iso(data,xmin=45,xmax=62)
data1=noKernel(data1,smooth=0.5);
data1=trim(data1,c=1.5);
data2=linterp(data1,dt=0.1);
###Determine nominal precession and eccentricity periods,then conduct nominal timeOpt analysis
targetTot=calcPeriods(g=c(5.525000,7.455000,17.300000,17.850000,4.257455),k=59,output=2);
targetE=sort(targetTot[1:5],decreasing=T);
targetP=sort(targetTot[6:10],decreasing=T);
###run nominal timeOpt and output sedimentation rate grid and fit
res1=timeOpt(data2,sedmin=0.1,sedmax=1.8,numsed=100,targetE=targetE,targetP=targetP,flow=1/22,fhigh=1/15,roll=10^7,limit=T,output=1);
###output optimal time series, bandpassed series, amplitude envelope and TimeOpt-reconstructed eccentricity
res2=timeOpt(data2,sedmin=0.1,sedmax=1.8,numsed=100,targetE=targetE,targetP=targetP,flow=1/22,fhigh=1/15,roll=10^7,limit=T,output=2);
###perform nominal timeOpt significance testing
simres=timeOptSim(data2,sedmin=0.1,sedmax=1.8,numsed=100,targetE=targetE,targetP=targetP,flow=1/22,fhigh=1/15,roll=10^7,numsim=2000,output=2,ncores=6);
###plot summary figure
timeOptPlot(data2,res1,res2,simres,flow=1/22,fhigh=1/15,fitR=0.12135,roll=10^7,targetE=targetE,targetP=targetP,xlab="Height(m)",ylab="Ca",verbose=T);
###run a single timeOptMCMC chain (50 chain)
```

```
res=timeOptMCMC(data2,sedmin=0.1,sedmax=1.8,sedstart=1.59,gAve=c(5.525000,7.455000,17.300000,17.850000,4.257455),gSd=c(0.12500,0.01500,0.150005,0.15000,0.00002),gstart=c(-1,-1,-1,-1,-1),kAve=59,kSd=5,kstart=-1,rhomin=0,rhomax=0.9999,rhostart=-1,sigmamin=NULL,sigmamax=NULL,sigmastart=1,nsamples=600000,
iopt=1,epsilon=c(0.2,0.2,0.35,0.35,0.8,0.85,0.6,0.35,0.9,0.35,0.9)/40,ran=T,burnin=-1);
### output the TimeOptMCMC results
write.table(res,file="Ma_Ca_470Ma_TimeOptMCMC_results.csv",sep=",",row.names=FALSE)

###### Data from Sorensen et al (2020 EPSL) S% (83-85.5m) time series (~493 Ma)
library(astrochron);
###Obtain the target dataset
Soren=read();
###Interpolate the data to the median sampling interval
Soren1=linterp(Soren,dt=0.01);
Soren2=iso(Soren1,xmin=83, xmax=85.5);
Soren2=trim(Soren2,c=1.5);
Soren2=linterp(Soren2,dt=0.02);
###Determine nominal precession and eccentricity periods,then conduct nominal timeOpt analysis
targetTot=calcPeriods(g=c(5.525000,7.455000,17.300000,17.850000,4.257455),k=59,output=2);
targetE=sort(targetTot[1:5],decreasing=T);
targetP=sort(targetTot[6:10],decreasing=T);
###run nominal timeOpt and output sedimentation rate grid and fit
res1=timeOpt(Soren2,sedmin=0.1,sedmax=0.4,numsed=100,targetE=targetE,targetP=targetP,
flow=1/22,fhigh=1/15,roll=10^7,limit=T,output=1);
###output optimal time series, bandpassed series, amplitude envelope and TimeOpt-reconstructed eccentricity
```

```
res2=timeOpt(Soren2,sedmin=0.1,sedmax=0.4,numsed=100,targetE=targetE,targetP=targetP,flow=1/22,fhigh=1/15,roll=10^7,limit=T,output=2);
###perform nominal timeOpt significance testing
simres=timeOptSim(Soren2,sedmin=0.1,sedmax=0.4,numsed=100,targetE=targetE,targetP=targetP,flow=1/22,fhigh=1/15,roll=10^7,numsim=2000,output=2,ncores=6);
###plot summary figure
timeOptPlot(Soren2,res1,res2,simres,flow=1/22,fhigh=1/15,fitR=0.18408,roll=10^7,targetE=targetE,targetP=targetP,xlab="Height(m)",ylab="S",verbose=T);
###run a single timeOptMCMC chain (100 chain)
res=timeOptMCMC(Soren2,sedmin=0.1,sedmax=0.5,sedstart=0.34,gAve=c(5.525000,7.455000,17.300000,17.850000,4.257455),gSd=c(0.12500,0.01500,0.150005,0.15000,0.00002),gstart=c(-1,-1,-1,-1,-1),kAve=59,kSd=5,kstart=-1,rhomin=0,rhomax=0.9999,rhostart=-1,sigmamin=NULL,sigmamax=NULL,sigmastart=1,nsamples=200000,
iopt=1,epsilon=c(0.2,0.2,0.35,0.35,0.8,0.85,0.6,0.35,0.9,0.35,0.9)/40,ran=T,burnin=-1);
### output the TimeOptMCMC results
write.table(res,file="Sorensen_S%_493Ma_TimeOptMCMC_results.csv",sep=",",row.names=FALSE)

### Data from Li et al (2022, Global and Planetary Changes) MS time series (570 Ma)
library(astrochron);
###Obtain the target dataset
Li=read();
### Interpolate the data to the median sampling interval
Li=linterp(Li);
Li_1=iso(Li,xmin=26,xmax=33);
Li_2=noKernel(Li_1,smooth=0.5);
Li_3=trim(Li_2,c=1.5);
Li_4=linterp(Li_3,dt=0.03);
```

```
###Determine nominal precession and eccentricity periods,then conduct nominal timeOpt analysis

targetTot=calcPeriods(g=c(5.525000,7.455000,17.300000,17.850000,4.257455),k=60,output=2);

targetE=sort(targetTot[1:5],decreasing=T);

targetP=sort(targetTot[6:10],decreasing=T);

###run nominal timeOpt and output sedimentation rate grid and fit

res1=timeOpt(Li_4,sedmin=0.5,sedmax=0.9,numsed=100,targetE=targetE,targetP=targetP,flow=1/21,fhigh=1/15,roll=10^7,limit=T,output=1);

###output optimal time series, bandpassed series, amplitude envelope and TimeOpt-reconstructed eccentricity

res2=timeOpt(Li_4,sedmin=0.5,sedmax=0.9,numsed=100,targetE=targetE,targetP=targetP,flow=1/21,fhigh=1/15,roll=10^7,limit=T,output=2);

###perform nominal timeOpt significance testing

simres=timeOptSim(Li_4,sedmin=0.5,sedmax=0.9,numsed=100,targetE=targetE,targetP=targetP,flow=1/21,fhigh=1/15,roll=10^7,numsim=2000,output=2,ncores=6);

###plot summary figure

timeOptPlot(Li_4,res1,res2,simres,flow=1/21,fhigh=1/15,fitR=0.1889,roll=10^7,targetE=targetE,targetP=targetP,xlab="Height(m)",ylab="MS",verbose=T);

###run a single timeOptMCMC chain (100 chain)

res=timeOptMCMC(Li_4,sedmin=0.5,sedmax=0.9,sedstart=0.77,gAve=c(5.525000,7.455000,17.300000,17.850000,4.257455),gSd=c(0.12500,0.01500,0.150005,0.15000,0.00002),gstart=c(-1,-1,-1,-1,-1),kAve=60,kSd=5,kstart=-1,rhomin=0,rhomax=0.9999,rhostart=-1,sigmamin=NULL,sigmamax=NULL,sigmastart=1,nsamples=200000,

iopt=1,epsilon=c(0.2,0.2,0.35,0.35,0.8,0.85,0.6,0.35,0.9,0.35,0.9)/20,ran=T,burnin=-1);

### output the TimeOptMCMC results

write.table(res,file="Li_MS_570Ma_TimeOptMCMC_results.csv",sep=",",row.names=FALSE)
```

References

61. F. Sun, W. Hu, J. Cao, X. Wang, Z. Zhang, J. Ramezaniet, S. Shen, Sustained and intensified lacustrine methane cycling during Early Permian climate warming. Nat Commun. 13, 4856 (2022).

62. C.R. Scotese, An Atlas of Phanerozoic Paleogeographic Maps: The Seas Come In and the Seas Go Out. Annual Review of Earth and Planetary Sciences. 49, 679-728 (2021).

63. B.J.W. Mills, C.R. Scotese, N.G. Walding, G.A. Shields, T.M. Lenton, Elevated CO_2 degassing rates prevented the return of Snowball Earth during the Phanerozoic. Nat Commun. 8, 1110 (2017).

64. J. Fang., H. Wu., Q. Fang., M. Shi., S. Zhang., T. Yang., H. Li., L. Cao., Cyclostratigraphy of the global stratotype section and point (GSSP) of the basal Guzhangian Stage of the Cambrian Period. Palaeogeography, Palaeoclimatology, Palaeoecology, 540 (2019).